INTERNATIONAL CENTRE FOR THEORETICAL PHYSICS
15 MAR 1983
LIBRARY

CONTENTS

INTERNATIONAL ATOMIC ENERGY AGENCY
UNITED NATIONS EDUCATIONAL, SCIENTIFIC AND CULTURAL ORGANIZATION

INTERNATIONAL CENTRE FOR THEORETICAL PHYSICS
34100 TRIESTE (ITALY) - P.O.B. 586 - MIRAMARE - STRADA COSTIERA 11 - TELEPHONES: 224281/2/3/4/5/6
CABLE: CENTRATOM - TELEX 460392-1

SMR/100 - 55

WINTER COLLEGE ON LASERS, ATOMIC AND MOLECULAR PHYSICS

(24 January - 25 March 1983)

PROBLEMS IN FAST FLUORESCENCE DETECTION

An application to molecular photophysics and photochemistry

J. LANGELAAR

Laboratory for Physical Chemistry
University of Amsterdam
Amsterdam
Netherlands

These are preliminary lecture notes, intended only for distribution to participants.
Missing or extra copies are available from Room 230.

I. MOLECULAR PHYSICS OF POLYATOMIC MOLECULES.

1. Introduction.

The past decennium has presented a tremendous increase of activity in the study of physical and chemical action of radiation. Short lived states and intermediates can now be routinely prepared by picosecond and subpicosecond lasers. Fluorescence emission spectroscopy is a common technique in molecular physics research. Picosecond luminescence measurements, however, have been developed only in recent years and is still not a standard technique in photophysical and photochemical research. Nevertheless photobiologists and biochemists have shown their interest in picosecond luminescence techniques in literature.

2. Absorption of light by molecules.

By absorption of light (UV and visible) a molecular species can be prepared in an electronic excited state.
Molecular absorption spectra are used for identification, to characterize the electronic levels of the molecule or to prepare a molecule in a certain excited state.
A fluorescence excitation spectrum is the most sensitive manner for identification and characterization of electronic levels. In this method the fluorescence emission is observed at a fixed wavelength.
Still the most commonly employed presentation of these spectra is a measure of (relative) intensity on the ordinate and the wavelength, energy or frequency function on the abscissa. It is adviseable, although not yet common, to present spectra linearly with respect to energy on the abscissa (in units of cm^{-1}) because the energy of and energy differences between molecular transitions are of fundamental interest.

In polyatomic molecules the electronic transitions belong to excitation of electrons in either n- or Π-orbitals within the chromophore groups. The electrons are then excited to Π^* antibonding orbitals and hence can be classified as n-Π^* and Π-Π^* transitions. (cf. the lecture notes of D.A. Ramsay)
Molecules with unsaturated groups (chromophores) like

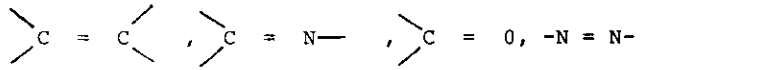

mostly absorp in the UV. The absorption is dependent upon the number, conjugation and position of unsaturated bonds in the molecule. n-Π^* transitions may shift the absorption spectrum to the visible like in aza benzenes (see I-4).

3. Characterization of electronic energy levels.

If only electronic energy changes as a result of a molecular transition, than just single lines would be observed as in atomic spectra. As known, the transitions are accompanied by changes in vibrational and rotational energy levels so that a series of bands are observed, for large molecules in solutions even spread out to very broad bands. From vibrational and rotational analysis of electronic transitions changes in the geometry of excited electronic states can be obtained. While a jump of an electron upon absorption of light occurs in approx. 10^{-16} s. and a molecular vibration period is of the order of 10^{-13} s. it is allowed to separate both transitions in first order (Born Oppenheimer separation).
The electronic transition probabilities are dependent on the level multiplicity and symmetry of the wavefunctions of the appropriate electronic states.
The absorption intensity gives a first measure of the transition probability. Hence the oscillator strength presents a first indication of the characterization of the electronic transition and can also be used to predict the radiative lifetime of the excited state.
A detailed description is given by Strickler and Berg [1].
A simple to use expression is:

$$\frac{1}{\tau_r} = 2900\ n^2\ \bar{\nu}_0^2 \int \varepsilon d\tilde{\nu} \quad (\tau_r \text{ in seconds})$$

where $\int \varepsilon\ d\tilde{\nu}$ is the area under the curve of molecular extinction coefficient plotted against wavenumber, $\tilde{\nu}_0$ is the wave-

number of the maximum of the absorption band and n is the refractive index of the solvent.
A rough but handy calculation of the radiative lifetime can be obtained with

$$\frac{1}{\tau_r} \sim 10^4 \; \varepsilon_{max} \quad (s^{-1})$$

So for Rhodamine 6G with $\varepsilon_{max} \approx 10^5$ one calculates a radiative lifetime of the order of 10^{-9}s.
If the molecule is excited to an unstable state, the molecule will dissociate and the fragments are dissipated with varying amounts of kinetic energy, not quantized, and the absorption band will not show a band structure.
If the transition is to a stable excited state, which transfers to an unstable state which dissociates, the spectra will be somewhat diffuse. This is named electronic predissociation.

4. Stationary molecular states.

A molecule can exist in various states, each characterized by a distinct energy and distribution of nuclei and electrons.
In first approximation the internal energy of a free molecule can be described by

$$E = E_e + E_v + E_{rot}$$

E_e= electronic energy
E_v= vibrational energy
E_{rot}= rotational energy

The wavefunction ϕ_i, characterizing a molecular state, is one of the stationary solutions of the Schrödinger equation. The energy E_i, a measurable physical property is known if the wavefunction ϕ_i is known. For organic molecules only approximate solution can be derived, where interactions are frequently neglected in the derived models (i.e. Born-Oppenheimer separation, Spin-orbit coupling, etc.). (For a more detailed description see the lecture notes of G. Amat).

5. Energy level diagram and transitions of S-Tetrazine.

S-Tetrazine $C_2H_2N_4$ (fig. 1.1) is a molecule of an iso-electronic family (homologous with benzene) of aromatic, nitrogen containing ring compounds: the azabenzenes.
For the understanding and interpretation of the spectra and fast fluorescence phenomena we will compare the MO description with benzene.
The MO-model is a naïve but instructive way of describing the electronic spectra of benzene and as we will see also for s-tetrazine. The LC-AO-MO treatment of benzene is described in many textbooks, in which the molecular orbitals are constructed from the six atomic Π-orbitals.
A similar approach for S-tetrazine is possible including the four pairs of nitrogen lone pair AO's.

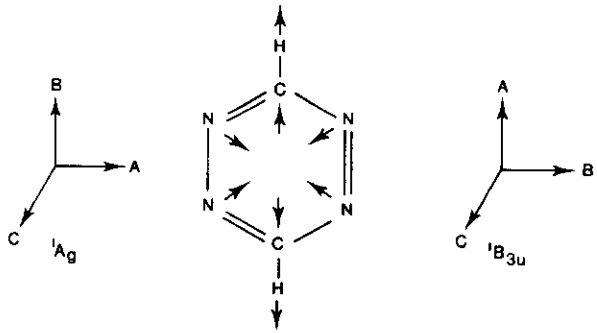

Fig. 1.1. Sym-tetrazine with inertial axes in ground and first excited singlet state. The arrows denote the geometry changes upon excitation to the S_1-state.

The zeroth order representation of the low lying electronic states of benzene and s-Tetrazine will be compared and discussed with the use of Fig. 1.2.

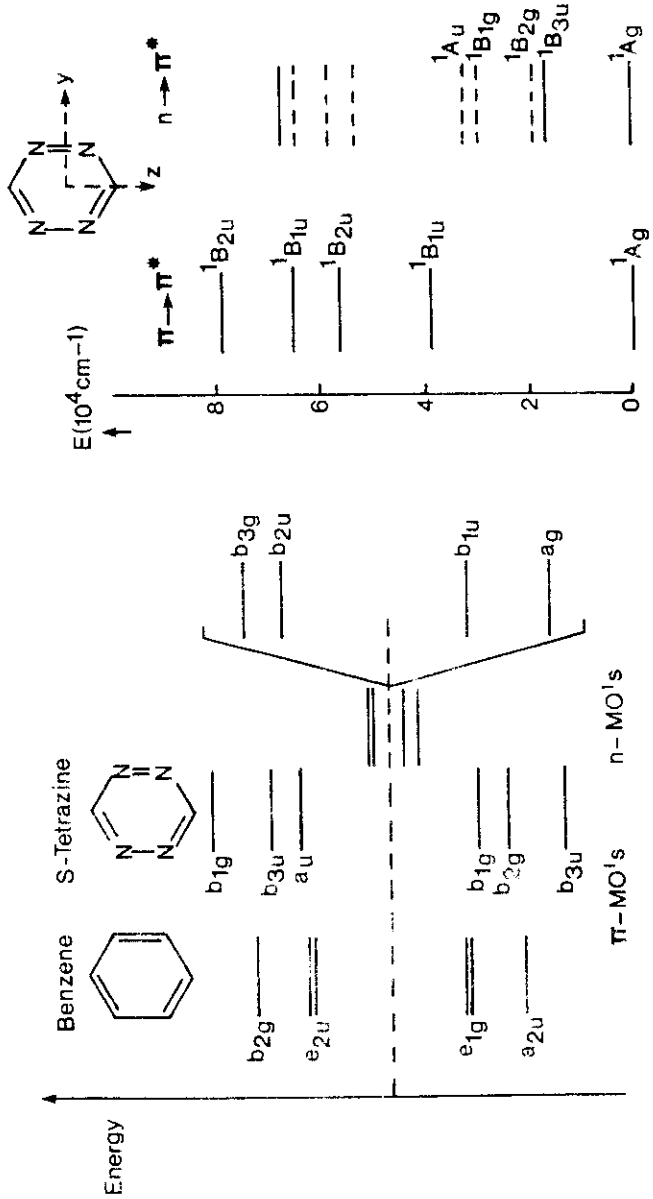

Fig. 1.2. MO level diagram of s-tetrazine

6. Transition moments and selection rules.

The energy level diagram of s-Tetrazine can be represented (as is the case for most aromatic molecules) by a Jablonski diagram. Optical transitions can take place between these levels by absorption or emission of light quanta. The different transitions, optical and radiationless, are indicated in fig. 1.3.

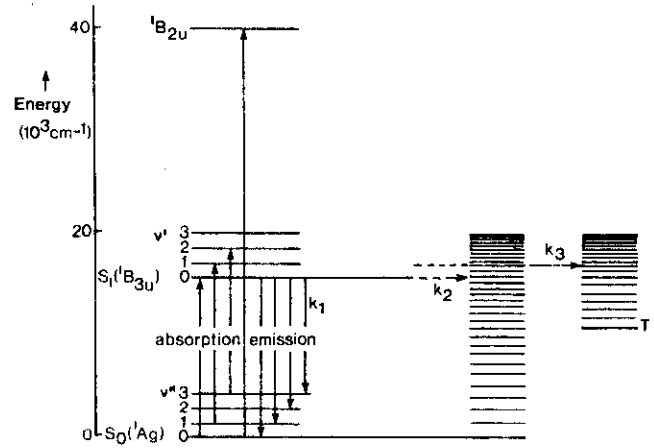

Fig. 1.3. Jablonski diagram for s-tetrazine. The rate constants k_i are described in chapter II.

The probability of the S_0-S_1 optical transition is proportional to the radiation density at frequency $\nu_{S_0 \to S_1}$ and to the square of the optical transition moment $|M|^2$; with

$$M = \langle \phi_{S_1} |P| \phi_{S_0} \rangle \quad ,$$

P being the operator working on ϕ_{S_0}, which is specific for the transition.

Symmetry considerations tell us whether this integral is zero or not. They are based on the symmetry of the wavefunctions and the operator.

The selection rules for the electronic and vibronic transitions of s-tetrazine will be discussed and compared with the observed spectra with the help of the simple LCAO-MO level scheme given in fig. 1.2. The absorption spectra are presented in fig. 1.4

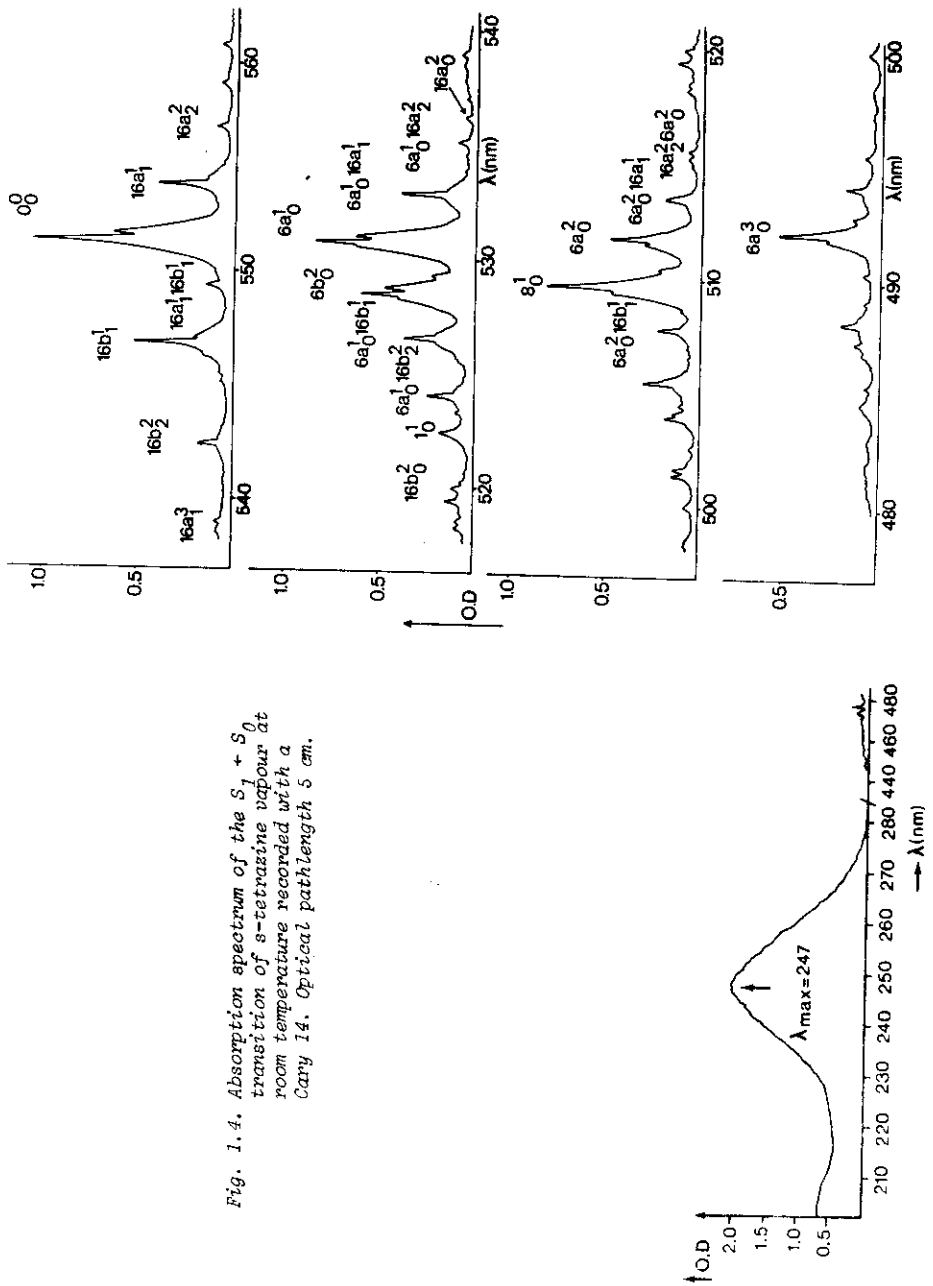

Fig. 1.4. Absorption spectrum of the $S_1 \leftarrow S_0$ transition of s-tetrazine vapour at room temperature recorded with a Cary 14. Optical pathlength 5 cm.

Examples for the $\Pi^* \leftarrow n$ transitions. Pointgroup D_{2h}

i) $\Pi^* \leftarrow n$, vibrationless $S_1 \leftarrow S_o$ transition

$\Gamma\phi^e_{S_o} = A_g$; $\Gamma\phi^e_{S_1} = \Gamma(n) \times \Gamma(\Pi^*) = b_{3g} \times A_u = B_{3u}$

Hence $|M| = \Gamma\phi^e_{S_1} \times \Gamma\begin{pmatrix}x\\y\\z\end{pmatrix} \times \Gamma\phi^e_{S_o} =$

$= B_{3u} \times \begin{matrix}B_{3u}\\(B_{2u})\\B_{1u}\end{matrix} \times A_g = \begin{matrix}A_g\\(B_{1g})\\B_{2g}\end{matrix}$

The totally symmetric representation is obtained: the transition is allowed in x-polarisation.

ii) $\Pi^* \leftarrow n$, transition $A_u \leftarrow A_g$ ($S_n \leftarrow S_o$):

$\Gamma\phi^e_{S_n} = \Gamma(n) \times \Gamma(\Pi^*) = A_g \times A_u = A_u$

Hence $|M| = A_u \times \begin{matrix}B_{3u}\\(B_{2u})\\B_{1u}\end{matrix} \times A_g = \begin{matrix}B_{3g}\\(B_{2g})\\B_{1g}\end{matrix}$

The totally symmetric representation is not obtained; the transition is forbidden. Participation of vibrations in the excited state of the required symmetry (B_{3g}, B_{2g}, B_{1g}) can make the transition allowed.

References:

(1) J. Strickler and R.A. Berg, J.Chem.Phys. 71, 4757 (1979).

II. FLUORESCENCE DECAY EXPERIMENTS

1. Kinetics.

Luminescence decay studies have been performed and improved in the last decennia from the time range of seconds to the femtosecond regime. Nearly every ten years an improvement in the time resolution of 3 orders of magnitude has been obtained.
Subsequent to excitation into the first excited state a molecule can luminesce or undergo various non radiative processes as internal conversion, intersystemcrossing and decomposition (see fig. 1.3).
The following mechanism will be discussed:

(2-1)	$M \xrightarrow{h\nu} M^*$	excitation
(2-2)	$M^* \xrightarrow{k_1} M + h\nu_F$	radiative transition
(2-3)	$M^* \xrightarrow{k_2} M$	internal conversion
	$M^* \searrow$ products	photodecomposition
(2-4)	$M^* \xrightarrow{k_3} {}^3M$	intersystemcrossing
(2-5)	$M^* + Q \xrightarrow{k_q}$ relaxation or products (collision induced)	

If the system is excited under isolated conditions by an optical δ-pulse than the decay will follow:

$$M^*(t) = M_0^* \exp\{-(k_1+k_2+k_3)t\} \qquad (2\text{-}6)$$

with M_0^* is the concentration of the excited state at t=0.
Then, the 1/e-lifetime is defined by

$$\tau = 1/(k_1+k_2+k_3) \qquad (2\text{-}7)$$

and the radiative lifetime by

$$\tau_r = \frac{1}{k_1}$$

The fluorescence quantum yield ϕ_F is obtained by

$$\phi_F = \frac{\tau}{\tau_r} = \frac{k_1}{k_1+k_2+k_3} \qquad (2\text{-}8)$$

The radiative lifetime τ_r can thus be obtained by measuring ϕ_F and τ.
In principle the above given description holds for molecules in any phase. For isolated molecules in the gas phase at low pressure, where the time between two collisions is long compared to the lifetime, we are able to study the radiative and non radiative transitions as a function of vibrational energy. On the other hand by adding collision partners it is possible to study relaxation processes in the one collision regime.
There are however practical problems: at a low vapour pressure we normally encounter low optical densities. Time-correlated single photon counting is a practically technique to study the dynamic properties of these systems.

For decay times of the order of 10^{-9}s. a maximum vapour pressure of about 10^{-3} bar has to be selected to study molecules under isolated conditions.
Equation (2-6) then describes the first order kinetics and eq. (2-7) presents the lifetime of the prepared state of the molecule. The decay times obtained for s-Tetrazine at 1 mbar vapour pressure are given in figure 3.4.
The fluorescence quantum yield is obtained with the help of eq. (2-8). For the 0^0 level we obtained a decaytime of 830 ps and a calculated radiative lifetime of 850 ns i.e.

$$\phi_F = \frac{830\cdot10^{-12}}{850\cdot10^{-9}} \approx 10^{-3}$$

2. Fluorescence decay techniques.

The techniques for measuring fluorescence decay times can be divided in phase shift methods and pulse methods.

2.1. Phase shift methods.

The phase shift method is based on excitation with modulated

light. The fluorescence will be shifted in phase with respect to the exciting light depending on the lifetime of the excited state. With help of a phase sensitive detection the decay times can be calculated. The method is a good alternative for the pulse methods, but will not further be discussed in the scope of this lecture.

2.2. Pulse methods.

a. Excite and probe method.
This method is based on the accurately known speed of light. An excitation pulse firstly prepares the molecules in the excited state. Then an interogating second pulse (probe) examines the system at a certain time delay. The recovery of the ground state molecules (as a result of fluorescence or internal conversion) can be obtained with this method as a function of time delay between the excite and probe pulse. The time delay is measured as an difference in optical pathlength, i.e.

$$3 \text{ mm} :: \frac{3.10^{-1}\text{cm}}{3.10^{10}\text{cm/s}} = 10^{-11}\text{s} = 10 \text{ ps}.$$

The method is described in more detail in the lecture of Prof. W. Kaiser.

b. Direct methods using ultra-fast detectors.
Since the developments of picosecond and subpicosecond laser pulse techniques , a δ-pulse excitationsource is available for most fluorescence studies to prepare a molecule in it's excited state, followed by a study of the emission as a function of time.
The measurement of the temporal intensity profile I(t) with picosecond time resolution and high sensitivity is the key to the study of dynamical processes in matter. The difficulty in obtaining high time resolution is often due to the low light level of the signal to be detected. High intensity ps laser pulses can be measured with measuring equipment having a short response time like Silicon photodiodes and streak cameras (see table I; first column).

Table 1. Detector response time and detection limits.

	Response to δ-pulse (ns)	transit time spread[1] (ps)	sensitive area (diameter)	detection limit (photons/event)
Si-photodiode	50ps	-	50µm	100
SPAD-photodiode	20	90	35µm	10^{-4} [3]
PM XP 2020	2.5	220	5mm	3.10^{-7}
X-Field	150ps	230[2]	5x6mm	10^{-6} [4]
M.C.P	0.9	70	18mm	10^{-4} [3]
Streak camera	2ps		0.025x5 mm	10 [3]
Synchroscan	10ps		0.025x5 mm	10^{-1} [3]

[1] measured by SPC; [2] preliminary, probably sofar limited by electronics; [3] calculated from literature values; [4] at -78°C.

(The optical methods: two photon fluorescence; measurement of autocorrelationfunctions with second harmonic generation etc. will not be discussed.)
The measurement of a (weak) fluorescence decay has to make use of a fast photodetector with high internal amplification and can be performed

(i) by measuring the waveform of the detector current pulse (by sampling and averaging techniques) or
(ii) by measuring the time position of the single photon response of the detector with respect to the excitation pulse and then accumulate many of such events in a hystogram.

The resolving time for averaging techniques is dependent on the delay of the arrival time of the photons at the photocathode of fast detector and on the jitter of this delay. Hence

$$\Delta t_{aver.} \simeq \sqrt{t_\delta^2 + t_s^2}$$

t_δ = response function of the detector amplifier
t_s = transit time spread

For time correlated single photon counting only the transit time spread contributes i.e.

$$\Delta t_{SPC} \approx t_s$$

So, the time resolution of the single photon counting method in combination with a fast photomultiplier is in favour of averaging and sampling methods.
We will discuss in the sections 4 and 5 of this chapter the streak camera- and SPC-technique (so called photochronoscopy) but first we will describe the excitation source well suited for these systems: the synchronously pumped picosecond dye laser.

3. Synchronously pumped cw dye laser system.

For a detailed description the author refers to the lecture notes of Prof. B. Wilhelmi. A description of authors system as used for the experiments presented in this lecture is given in the following reprint of a letter in Optics Communications (1976).
The linewidth of the tunable ps-pulses around 550 nm can now be selected between 30 cm^{-1} (∿1ps) and 0,03 cm^{-1} (∿800 ps).

Reprint from Optics Communications, Vol. 18, nr. 1 (1976) 24-26.

C8 **GENERATION OF 530–670 nm AND 265–335 nm PICOSECOND PULSES IN A CW DYE LASER BY MODE-LOCKED SYNCHRONOUS PUMPING**

J. de VRIES, D. BEBELAAR and J. LANGELAAR
University of Amsterdam, Laboratory for Physical Chemistry, Nieuwe Prinsengracht 126, Amsterdam, the Netherlands

A number of approaches has been published to produce tunable picosecond pulses by mode-locking a cw dye laser with Rhodamine 6G as the lasing dye. We have chosen for the method of synchronous pumping by a mode-locked argon-ion laser [1,2]. This approach gives a system that is easier to operate, which is especially important when frequency doubling of the dye laser pulses is used. The 1.5 m argon-ion laser (CR-5) is mode-locked by an acousto-optic loss modulator. The output at 514.5 nm consists of a train of pulses (90 ps FWHM) at 94.6 MHz with an average power of 1.1 W. The cavity of a jet stream dye laser (Cr-490) was extended to 1.5 m and matched to the repetition frequency of the pump pulses by displacing mirror M_3 (fig. 1).

The duration of the dye laser pulses was measured with a Michelson interferometer and a KDP crystal using the well known SHG [illegible] depended very critically on the [illegible] cavity length [illegible] mode-locked [illegible] determined [illegible]

Lyot-filter for Rhodamine 6G a pulse duration of 7.5 ps and a bandwidth of 80 pm (0.8 Å) is observed. This performance is transform limited assuming a gaussian pulse shape ($\Delta\nu \Delta t \approx 0.52$). For a 2-elements Lyot-filter we obtained 4.5 ps and 220 pm.

In the literature [2] it was suggested that the optical pulse should consist of two pulses 330 ps apart (i.e. twice the distance dye-sheet M_1). Although the detection system is fast enough (fig. 2) to separate the two pulses we observed that only one pulse travels in the dye laser cavity. The time delay between the pump pulse and the dye laser pulse in the dye sheet depends on the adjustment of the cavity length. When the mode-locking is at optimum the pulse [illegible] the dye sheet in the direction of [illegible] 330±50 ps later [illegible]

For Rhodamine B, 6G and sodium fluorescein (530–670 nm) typical average output powers are given in fig. 3. It was observed that the pump threshold for lasing in mode-locked operation (200 mW) is four times lower than with cw pumping (800 mW). Average output powers of generated uv picosecond pulses between 265 and 335 nm are given in fig. 3 as well. With angle tuned KDP crystals an energy conversion of about 0.05% is obtained. With a 90° phase-matched ADP crystal much higher efficiencies are found. Around 270 nm we measured a conversion efficiency of 2% and may thus expect for Rhodamine 6G with a 90° phase matched ADA crystal an average mode locked uv output power of at least 5 mW.

The obtained tunable picosecond pulses at high repetition rate are very attractive for the study of spectrally resolved dynamic processes in molecules. Even in the uv region (fig. 3) the energy per pulse (10^5 10^6 photons) is sufficient to measure fluorescence decays in the ps and ns time range with the single photon counting technique. Results obtained for organic molecules at low vapour pressures will be discussed. For example for s-tetrazine at 10^{-1} torr decay rates between 2×10^9 and 8×10^8 sec^{-1} are obtained depending on the vibronic level excited.

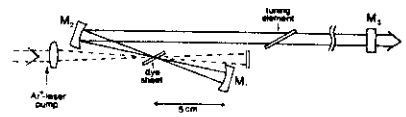

Fig. 1. Configuration of mode-locked cw dye laser.

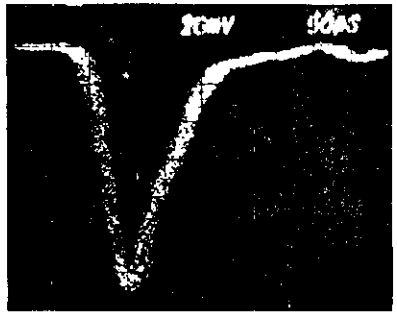

Fig. 2. Detector limited mode-locked dye laser pulse observed with a fast photodiode (fwhm = 90 ps) and a sampling oscilloscope (50 ps/div).

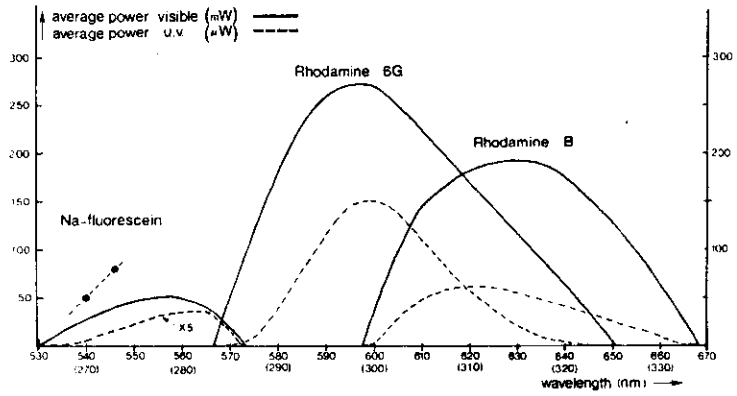

Fig. 3. Tuning curves of mode-locked average power for three different dyes. Tuning element: 3-elements Lyot filter. Average pump power at 514 nm: 1.1 W. Pulse duration: 7.5 ps at 600 nm. —— average power visible output in mW, – – – average power uv output in μW with angle tuned KDP crystals, –·–·– ibid with 90° phase matched ADP crystal.

REFERENCES

1. C.K. Chan and O. Sari, Appl.Phys.Lett. 25 (1974) 7.
2. J.E. Harris, [illegible] tle, Appl.Phys.Lett. 26 (1975) 1.

4. Streakcamera photochronoscopy.

The streakcamera, the use of which was already suggested in 1956, is one of the few instruments that can directly measure the time versus intensity profile of a picosecond optical event. It can produce a linear and real time measurement without the need for deconvolution or curve fitting.
The main part of the streak camera is the electron optical streak tube, the operation of which is presented in fig.2.1. The incident optical signal is first directed onto a slit and is subsequently imaged onto the photocathode of the streak tube. The optical signal generates photoelectrons which are accelerated at high potential and focused onto the phosphor screen of the streak tube. The intensity of slit image on phosphor is proportional to the intensity of the incident optical signal. By applying a time-varying high voltage to the streak tube deflection plates, it is possible to deflect the image across the phosphor screen, thus generating a time-intensity profile of the optical signal. The distance displacement of the streak image is directly related to time, while the image intensity represents the optical signal intensity.

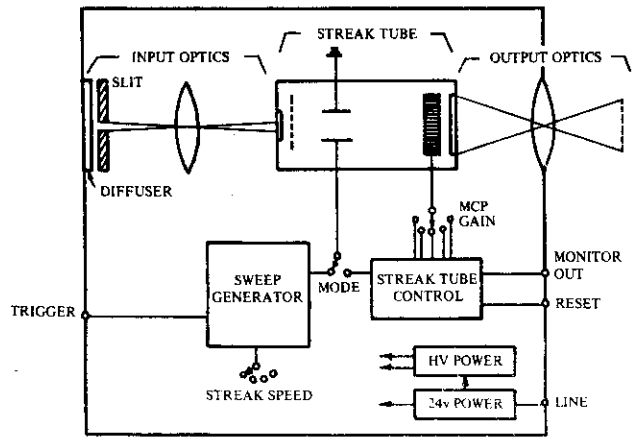

Fig. 2.1. Block diagram of a streak camera.

The time resolution of the streak camera is determined by photoelectron time dispersion as well as the image deflection velocity and spatial resolution of the streak tube.
Let us first consider the photoelecton time-dispersion effect. Because of pair production and lattice-scattering mechanisms in the photocathode, photoelectrons are emitted with a distribution of velocities. The effect is small when the incident optical signal has a wavelength near the photocathode cutoff but becomes more pronounced with shorter incident wavelengths. The distribution in initial photoelectron energy and velocity gives rise to a distribution in the transit times of the photoelectrons through the streak tube. This causes a broadening in the streak trace and a loss in temporal resolution. The spread in transit times may be written

$$t_d = m\Delta v/eE$$

Δv is the distribution of initial photoelectron velocities, e/m is the charge/mass of the electron and E is the electric field at the photocathode.

The more rapidly the electrons are accelerated to high velocity, the faster they forget their initial velocity distribution. The initial photoelectron velocity distribution is a function of both photocathode type and incident wavelength but typically $\Delta v \sim 2 \times 10^7$ cm/sec. Modern streak tubes such as the Photochron II or IV can produce extraction fields of 10-20 kV/cm so the typical photoelectron transit time spreading is < 1-2 ps.

Let us next consider the role of the deflection velocity and the spatial resolution in the time resolution of the streak camera. These factors, neglecting photoelectron dispersion and nonlinear saturation effects, determine what is termed the technical time resolution of the streak camera. Consider the streak image of an input optical signal consisting of two short pulses separated by an arbitrarily small delay time

Δt. The distance separation to the streak images on the phosphor screen of the streak tube is determined by the deflection velocity V_s to be $\Delta d = \Delta t V_s$. The resolvability of the two pulses will be governed by the dynamic spatial resolution of the streak camera and thus is:

$$t_T = 1/RV_s$$

Through the use of high-voltage Krytron switches, writing speeds of up to 2×10^{10} cm/sec have been obtained.

With the use of higher streak speeds the output image intensity at the phosphor screen of the streak tube decreases because the photoelectrons become dispersed over a larger area. Unfortunately if the incident optical signal intensity is increased the streak tube image becomes defocused. In order to avoid this parasitic effect, the photoelectron densities must be maintained below what is termed the photocurrent limit. The causes of this limit are not well known. The problem has in part been circumvented through the use of image intensifiers to process the streak image before recording. Early experimental systems employed a large and messy magnetically focused cascade intensifier for this purpose, however, later schemes used higher efficiency and less bulky fiber-optically coupled microchannel plate intensifiers . Some modern streak tubes incorporate the intensifier directly as a part of the streak tube.

In the absence of saturation effects, the streak camera response is determined mainly by the technical time resolution and photoelectron dispersion. The streak response to a laser pulse of duration t_p is thus:

$$t_R = \sqrt{t_d^2 + t_T^2 + t_p^2}$$

assuming gaussian profiles. Experimental time resolutions of < 2ps have been demonstrated.

We note that the spectral sensitivity range of the streak camera has been greatly extended through the use of different photocathode materials. The use of an S1 photocathode provides sensitivity down to wavelenght of $\sim$ 1200 nm, while good photocathodes function well into the UV.

The image intensification is performed by a microchannel plate electron multiplier.The microchannel plate consists of numerous electron channels bored into the plate and coated with a high resistance material having secondary electron emission.
By applying a high voltage bias to the opposite sides of the microchannel plate, a potential gradient is produced along the channel. A photoelectron incident into the channel will thus collide with the walls to produce secondary electrons which will be accelerated by the potential and undergo further multiplication. Finally the electron groups leave the channels and impinge on a phosphor output screen where they form an intensified version of the input image. The spatial resolution is $\sim$ 20 lp/mm.

The gain of the intensifier is determined by the biasing voltage across the channel plate as well as by geometry of the channels. Gains of approximately 10^2 to 5×10^4 are obtained depending on the bias voltage.

The streak camera and intensifier measure the time versus intensity variation of a picosecond event by producing a corresponding distance versus intensity variation in the streak image. An Optical Multichannel Analyzer (OMA) functions to record the optical output of the streak camera and convert it into usable digital form.

Figure 2.2 shows the time intensity profile with a camera set at the maximum writing speed for a set of pulses separated by 67 ps.

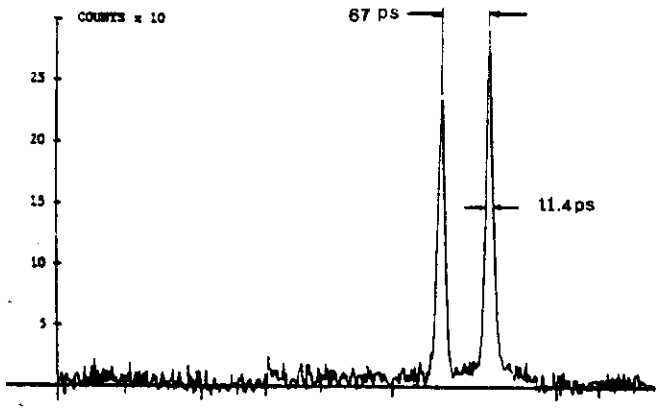

Fig. 2.2. Streak camera trace of two pulses separated by 67 ps.

To facilitate the recording of periodic low-intensity signals generated by cw modelocked lasers, the streak traces may be superimposed, allowing the signal to be integrated directly on the phosphor screen of the streak tube. The high data-accumulation rate provides a substantial increase on sensitivity and dynamic range over single-event streak cameras while allowing direct and linear measurement of the time-intensity variation of the optical event.

Synchronously operating streak cameras are provided by using a synchronized repetitive high-voltage deflection signal to the streak tube.
The minimum sensitivity of the streak camera (10^{-19}J)dynamic range ($\sim 10^3$) and system time resolution (1-25 ps) will be discussed. Also a fluorescence decay experiment will be presented.

Streak cameras provide the shortest resolving times of all electronic methods i.e.down to $\sim$ 1 ps.
The method still has some drawbacks:

- the resolving time is proportional to the time range scan
- the linearity is not high
- the equipment is expensive and not easy to operate
- the minimum sensitivity lies around 1 photon per event.

If such a high time resolution is not needed (i.e. not possible in high resolution spectroscopy) or if weak signals over a long time range have to be measured the S P C method (next section) has to be preferred.

5. Single photon counting photochronoscopy.

5.1. Fluorescence detection and signal processing.

Fluorescence signals have to be observed via a high resolution monochromator (preferably with two exit slits) if high spectral resolution and time resolution has to be combined. This system then also enables one to perform absolute calibration of the dye laser wavelenght and linewidth before and after each decay experiment. Most of the time resolved experiments in our lab were carried out with a Philips XP 2020 photomultiplier and a single photon counting system (SPC). The time resolution of this combination allows to measure decay times down to 100 ps without the need of convolution techniques. The usefulness of the SPC is due to its linearity high dynamic range and good signal to noise ratio in combination with an extremely high sensitivity. It allows decay time measurements of signals as low as 25 counts per second; the pulse repetition rate of the laser being 85 MHz. These are realistic signal levels encountered in our study on single level decay measurements of s-tetrazine vapour.
A block diagram of the excitation and the detection system is shown in fig. 2.3. The single photon counting electronics consist of standard Ortec modules. The Constant Fraction Discriminator has been selected to give lowest jitter (about 20 ps FWHM) and walk (25 ps peak to peak over a 20 dB range). The apparatus is used with the start and stop reversed. In this mode the start pulse going to the Time to Amplitude Converter (TAC) is delivered by the PMT and the stop pulse is derived from the laser pulse repetition rate. The TAC produces an output pulse with a height proportional to the time interval between a start and stop pulse. A Multi Channel Analyser (MCA)accumulates the pulses from the TAC. The display of the MCA will be a histogram of the detected photons in time which is equivalent to the fluorescence decay curve.

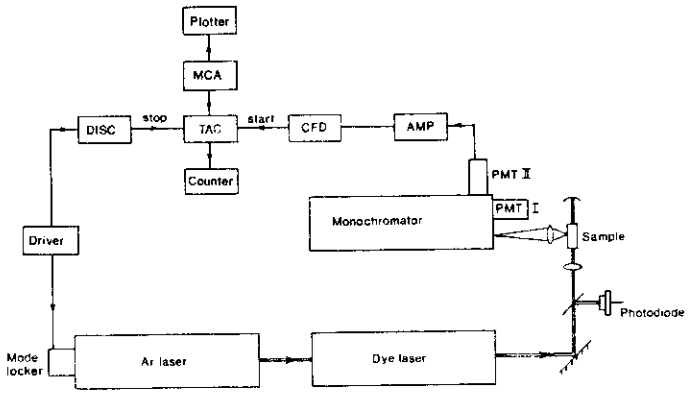

Fig. 2.3. Set-up for measuring decaytimes ≤ 2ns. PMT, photomultiplier (I:EMI 9558 QA, II:Philips XP 2020); CFD, constant fraction discriminator; TAC, time to amplitude converter; MCA, multichannel analyser.

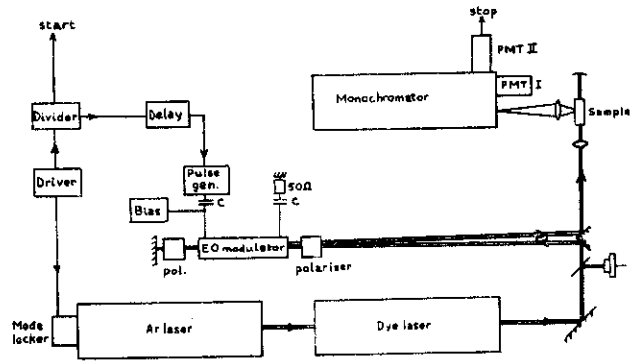

Fig. 2.4. Set-up for measuring decay times with large time window.

The maximum time interval during which the fluorescence decay can be viewed is the period between the laser pulses and is in our case 10 ns. In order to obtain an accurate interpretation of the decay curve over at least three decades, we accumulate in the MCA to 10^4-counts at the top of the decay curve. For SVL studies on s-tetrazine a measurement normally takes less than 1 minute counting time; for weak SRL studies with a signal level of 25 cps the operating time increases to 1 or 2 hours.

For decay times > 2 ns a low voltage electro-optic modulator is employed to decrease the repetition rate of the dye laser. This enables one to record the fluorescence decay with a time window larger than 10 ns.

The modulator power supply and the start pulses to the TAC are synchronized by dividing the modelocker drive frequency of the ion laser. The PMT-signal then delivers the stop pulses. The start pulses start the time-to-amplitude converter (TAC). If a stop pulse arrives within a preset time after the start, the TAC supplies an output pulse with a height proportional to the time interval between start and stop. The pulse serves as input to the multichannel pulseheight analyser and in this way a photon counting histogram of accumulated counts (ordinate) versus time (abscissa) is obtained. Conversion to absolute time is done by calibration using a pulsegenerator with known repetition frequency (Ortec Model 462 Time Calibrator). A scheme of the standard SPC configuration is given in fig. 2.4.

One of the problems of this technique for long decaytimes (pile-up) originates from the TAC. Once a stop pulse has been arrived within the pre-set time window, the TAC cannot detect a second stop pulse in the same time window.

Pile-up can be removed by surpressing measurements in which multiple stop pulses occur. For a continuous light source an estimate can be made on the basis of Poisson-statistics.

$$W(0) = e^{-\alpha}$$
$$W(1) = \alpha e^{-\alpha}$$
$$W(\geq 2) = 1 - e^{-\alpha}(1 + \alpha)$$

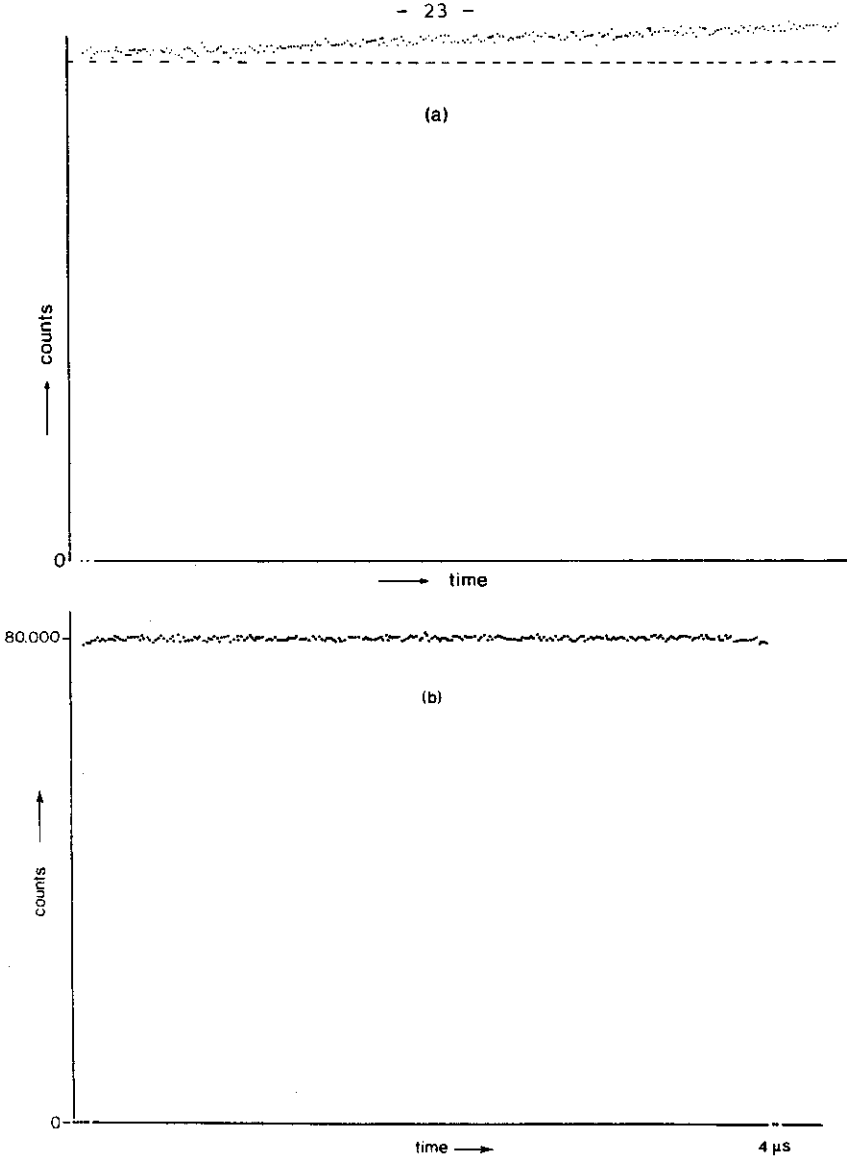

Fig.2.5 Adressing of photon counts for a constant light source at a rate of about 0.3 count per measurement. (a) : "anti" pile-up (see text for explanation). (b) : performance of the system.

W(0), W(1) and W($\geq$ 2) are the probabilities for zero, one and two (or more) stop pulses within the time window, respectively The quantity α is the mean number of stop pulses in the time window. Pile-up distortion is negligible when W($\geq$ 2)<<1, say 10^{-3}. Then α is known and fixes W(1).
Pile-up distortion can be much better surpressed by a device which counts the number of stop pulses in the time window of the TAC: when two stop pulses are couted, storage of the TAC output pulse in the multichannel analyser is prohibited.
With this pile-up inhibitor it is allowed to maximize W(1). Then α=1 and W(0) = W(1) = 0.37, i.e. the stop frequency may be just adjusted to 0.37 count per measurement.
Fig.2.5a shows the result for a constant light source. Clearly, a kind of "anti" pile-up is present. It turns out that for the time window (1 to 4 µs) and repetition frequency (100 kHz) used, the busy time of the multichannel analyser is responsible for this distortion (i.e. sometimes the TAC supplies a pulse while the multichannel analyser is not ready with the storage of the previous one). The distorsion is removed by prohibiting measure-

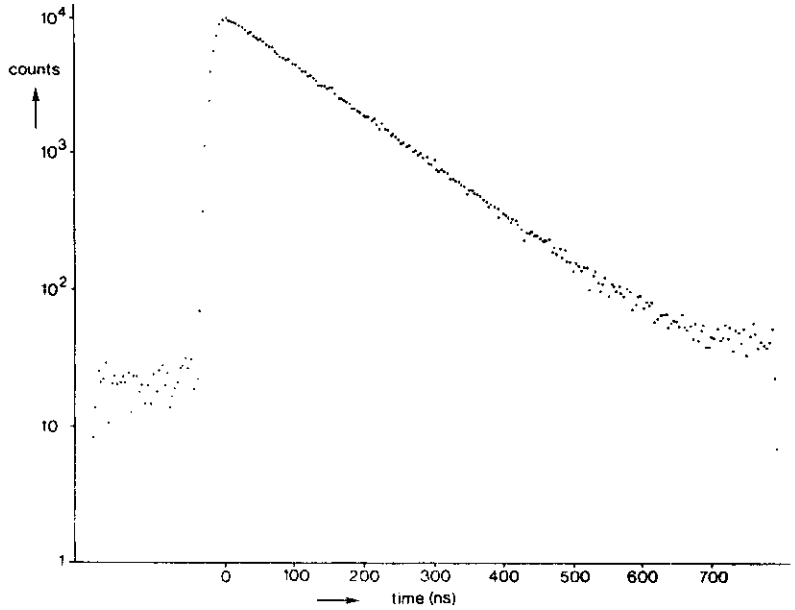

Fig. 2.6. Broad-band detected emission of I_2.

ment during the busy time of the multichannel analyser. Fig.2.5b shows the final result. No pile-up is [illegible] 30,000 counts per channel at any ratio of stop frequency to start frequency.
A typical result for the broad band detected emission of I_2-vapour is presented in fig. 2.6.

5.2. The photomultiplier tubes (PMT).

The response of the apparatus to a delta pulse has been measured as a function of wavelength for several photomultiplier tubes. The results are shown in fig.2.7 for a Philips 56 DUVP and a XP 2020 tube. A half-width of 620 ps is observed with the 56 DUVP, a widely used tube in single photon counting systems in the past. The response, however, changes considerably by going to shorter wavelength. The best results we have obtained so far are with the XP 2020 and are only slightly dependent on wavelength (curve b, fig.2.7).

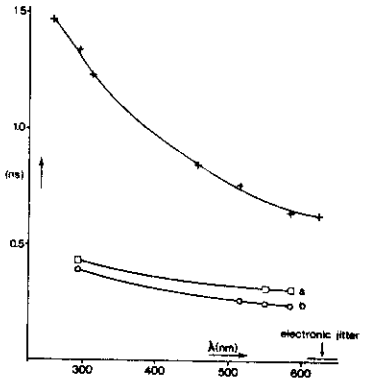

Fig. 2.7. Wavelength dependence of the photomultiplier response (FWHM) to a delta pulse: +, Philips 56 DUVP; □, Philips XP 2020(a); 0, Philips XP 2020, but after selecting the fastest area of the photocathode (b). The total electronic jitter is 15 ps.

The contribution of the first dynode to the response can be decreased by changing the operating voltages and then selecting the fastest area on the photocathode so that the transit time spread of the photo electrons is at a minimum. This gives an overall instrumental response of 230 ps (FWHM) at 580 nm. The results are reviewed in table 2. By using a special model Cross field photomultiplier we expect a further improvement of the instrumental resolution to 20-50 ps FWHM.

Table 2. Photomultiplier response

Type	photo-cathode	field-strength at cathode (V/cm)	time resolution FWHM (ps)			
			measured		estimated photo-cathode	estimated contribution first dynode
56 DUVP	bialkali (K_2CsSb)	40		620	540	290
XP 2020	"	180	a	320	120	290
			b	220	120	190
X-field PM	GaAs	2000		230[1]	20-50	

[1] *preliminary; probably limited by CFD electronics.*

Some of the decay results presented in the last chapter are performed with a Cross-Field photomultiplier.
The response function of the XP 2020 PMT to a delta pulse at λ=585 nm is given in fig. 2.8.

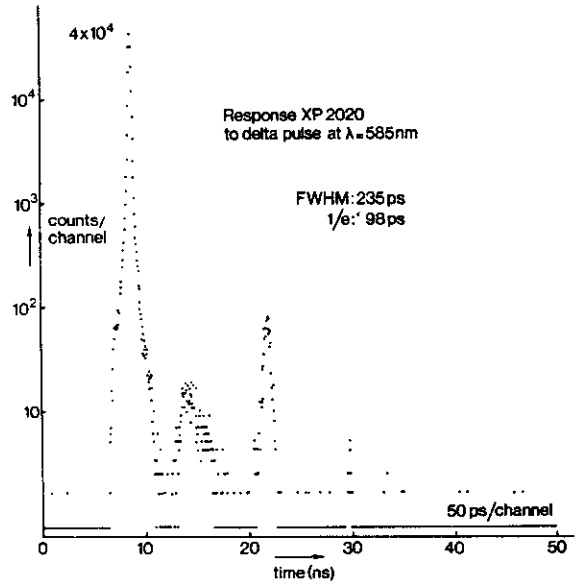

Fig. 2.8. Response function of the XP 2020 photomultiplier to a δ-pulse of λ = 585 nm.

Note that the ordinate is a logarithmic scale. The "afterpulses" are at least 3 orders of magnitude smaller than the main signal. The respons function shows a signal with a half-width of 235ps and a 1/e-decay of 98 ps.

The afterpulses around t ≈ 14 and 22 ns, are due to processes in the photomuliplier; the weak pulses around 20 and 30 ns are the next pulses from the dye laser indicating an extinction ratio of the modulator of at least 10^4.
The PMT response for the SPC system when the start and stop pulses are reversed is given in figure 2.9. at λ=546 nm. This response function is used to analyse the fluorescence decay time of Erythrosine B in this wavelength area.

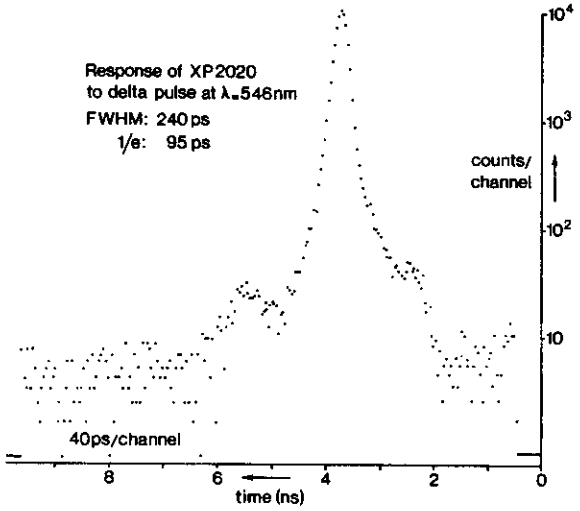

Fig. 2.9. Response function of XP 2020 to δ-pulse at λ=546 nm. Start and stop pulses are reversed.

5.3. Fluorescence decaytime of Erythrosin B.

Erythrosine B is a iodine substituted fluorescein dye from which is known, that the fluorescence yield is drastically reduced by going from acetone (0.5) to water (0.02) as solvent.
In acetone we observed a decaytime of 2.28 ns, which indicates a quantum yield of approximately 0.57 using a radiative lifetime of 4 x 10^{-9}s.
The results obtained from Erythrosin B in methanol and water are given in fig. 2.10. In methanol the decaytime τ = 460 ps, can directly be obtained from the logarithmic plot as given in fig. 2.10a.

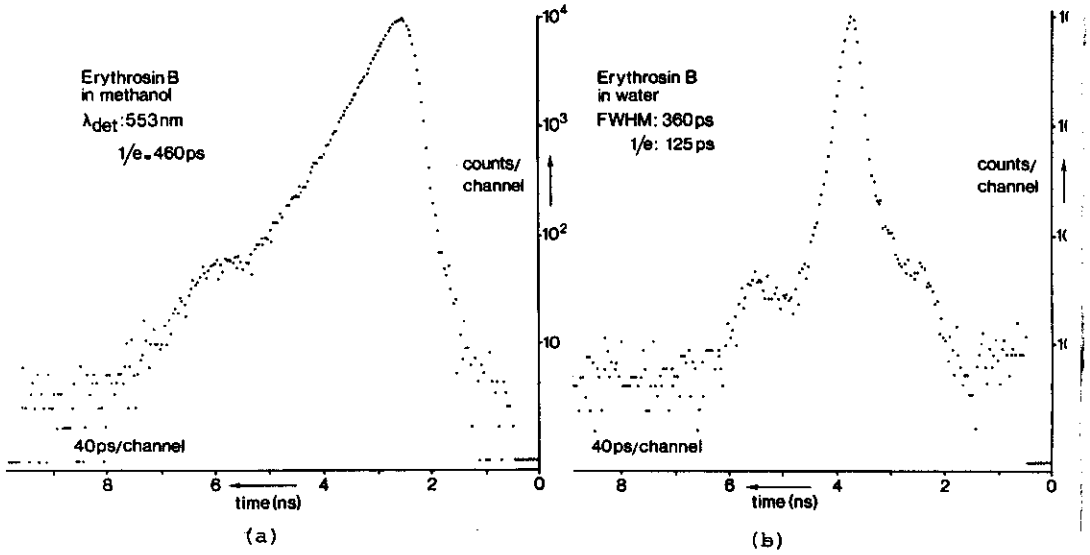

Fig. 2.10. Fluorescence decay curves of Erythrosine B in methanol (a) and water (b) measured by the single photon counting technique; τ_f(methanol) ≈ 460 ps; τ_f (water) < 125 ps.

Erythrosin B solved in water, however, gives a fluorescence intensity profile which slightly differs from the response function of the detector as given in fig. 2.8.

The 1/e-decay indicates a decaytime of $\tau<125$ps. A full convolution of the fluorescence intensity profile versus time of Erythrosin B in water with the equipment responsefunction gives a lifetime of $\tau=80 \pm 5$ps. The convoluted profile, with a decaytime of 80 ps, of the experimental intensity profile of Erythrosin B in water as obtained in fig. 2.10 is presented in fig. 2.11.

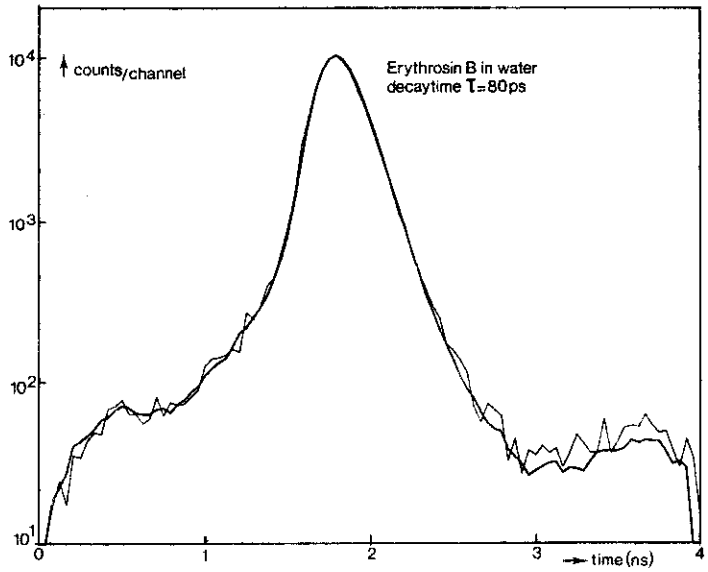

Fig. 2.11. Fluorescence decay curve of Erythrosin B in water. Thin line: part of the experimental curve of fig. 2.10b (100 channels). Fatline: intensity profile calculated with a decay time of 80 ps and the detector response function of fig. 2.9.

6. Monochromator time dispersion.

In many spectroscopic applications it is desirable to measure the time evolution of a given portion of a complicated emission spectrum. Special care is required when using a monochromator for time-resolved spectroscopy because it produces a temporal broadening in the optical signal. For a grating monochromator the origin of this broadening effect lies in the diffraction process itself. If a light wave is diffracted in first order from a grating, there must be a one-wavelength delay between rays reflected from

successive grating rulings. Thus if there are N grating grooves the time dispersion produced in the diffracted beam in first order is:

$$\Delta t = N\lambda/c \qquad (2\text{-}9)$$

Typical 1/4-m and 1/2-m monochromators employ 5-cm square gratings with $\sim$ 500 lines/mm and $\sim$ 1200 lines/mm respectively. For an incident signal at 6000 Å the resulting time dispersion is $\sim$ 50 ps and $\sim$ 120 ps.

There are two basic approaches for reducing the time dispersion produced by grating monochromators. The first approach is to decrease the number of grating grooves, N. The time dispersion is then reduced since it is proportional to N. The number of grating grooves may be reduced either by using a coarser grating with fewer lines per millimeter or by masking a portion of the grating, thereby restricting the aperture and exposing fewer rulings. While this solution is simple to implement, it has the disadvantage of decreasing the resolution of the monochromator. In particular, the resolving power of the grating is also proportional to the number of rulings:

$$\lambda/\Delta\lambda = N \qquad (2\text{-}10)$$

Thus there is a trade-off between the time dispersion and resolving power. This can be expressed by combining equations (2-9) and (2-10) to yield the familiar uncertainty relation limit:

$$\Delta\nu\Delta t = 1 \qquad (2\text{-}11)$$

The second approach for reducing the time dispersion consists of compensation for the diffraction process rather than adjusting N. It must be stressed that eq. (2-11) gives only a lower limit, achieved at minimum slit width ($\sim$ 5µm). Under practical experimental conditions with opened slits $\Delta\nu\cdot\Delta t$ might be as high as 100 or 1000. The compensation may be accomplished by employing a

special double grating monochromator as shown in fig. 2.12. The second grating functions to bring the time dispersion introduced by the first grating back to the theoretical limit. Consider a short pulse of light which is directed through the entrance slit of the monochromator. The ray at one side of the grating will travel a shorter path compared to one depicted on the opposite side. The wavefront of the light beam as indicated in the figure at the entrance slit will be tilted at the exit slit i.e. one side of the beam has been delayed with respect to the other side. With an identical monochromator as a compensator the inverse process occurs at the second grating. The optical path lengths from the entrance slit of the monochromator to the exit slit of the compensator are thus equal, regardless of where the ray is diffracted on the gratings. It is worth noticing that this is not a standard double monochromator.
The advantage of the use of a compensator overa reduction of the number of grooves is a higher throughput of light when the slits are opened wide.

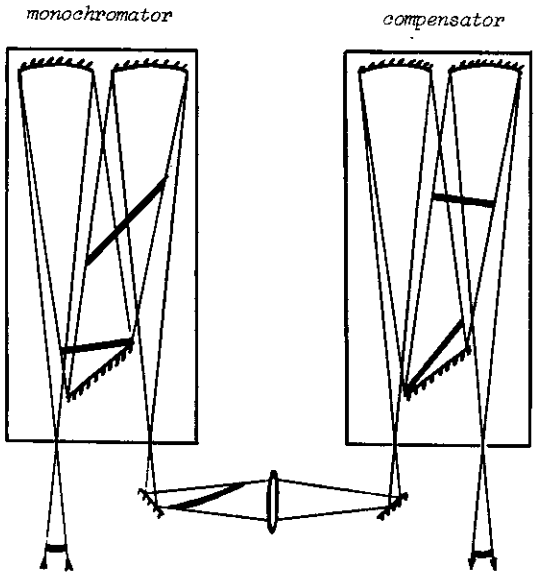

Fig. 2.12. Compensated monochromator

It is interesting to note, however, that the spectral resolution is limited by the duration of the optical signal. This arises because a short optical pulse has a limited spatial as well as temporal extent and only interacts with a small area of the grating at any instant. The effective number of grating rulings that the pulse diffracts from is reduced in proportion to its temporal duration. Thus the duration of the optical signal and the spectral resolution obtainable are inversely related.

III. SPECTROSCOPY OF S-TETRAZINE VAPOUR.

1. Fluorescence of isolated molecules.

Considerations of the first order kinetics of an isolated molecule (no collisions during the excited state lifetime) are given in chapter II . To study the kinetics of single vibrational levels of s-tetrazine the absorption and emission spectra should be known in great detail. In the absorption spectrum (fig. 1.4) we mainly observe progressions of the totally symmetric vibration 6a.
Further we observe a number of sequences around the origin due to hot bands of the 16a and 16b modes, which have a large Boltzmann factor at room temperature.
Some of the normal modes and their frequencies in ground and excited state are presented in Appendix A.

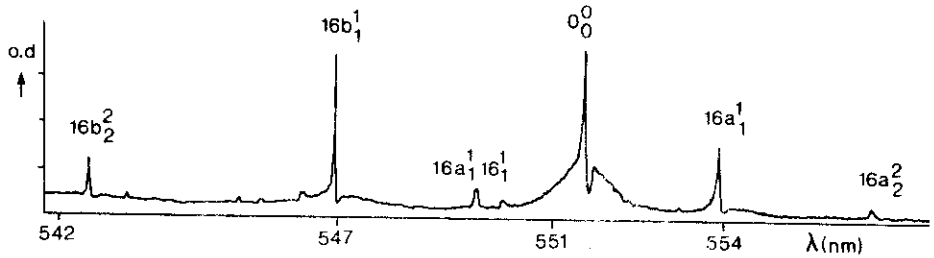

Fig. 3.1. Part of the laser-induced absorption spectrum of isolated s-tetrazine vapour (P=0.5 Torr). Assignments have been given in the figure.

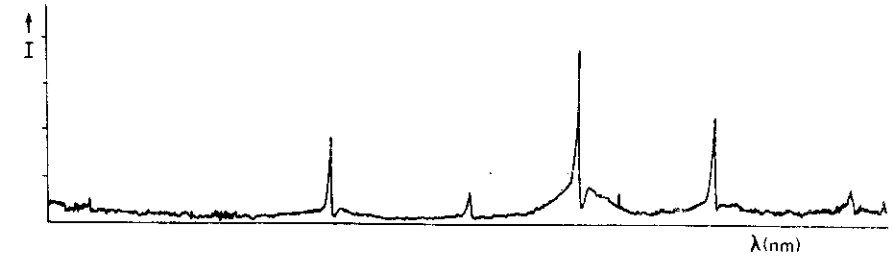

Fig. 3.2. Part of the fluorescence excitation spectrum corresponding with the absorption spectrum of fig. 3.1.

The laser induced absorption spectrum with a resolution of $\sim 0.8\ cm^{-1}$ in the neighborhood of the origin of the $^1B_{3u} \leftarrow {}^1A_u$ electronic transition is given in fig. 3.1.
For comparison we also present the fluorescence excitation spectrum (fig. 3.2) in the same spectral region. Both results are to be compared with the absorption spectrum of fig. 1.4.
Single vibronic level transitions are well separated in these spectra. Only a much higher spectral resolution enables one to resolve the rotational structure of the vibronic bands.
S-Tetrazine, being a large molecule, has a large Doppler width ($0.024\ cm^{-1}$ at $T \approx 300K$) and a short decay time, so that complete resolution of the rotational structure is excluded.
Single vibronic level emission spectra of isolated s-Tetrazine can be obtained after preparing the molecule in its first excited singlet state by the appropriate vibronic transition.
The emission spectra of the $16a^1$, $16b^2$ and $6a^1$ level are represented in fig. 3.3, examples of the detailed knowledge of the photophysics of the s-Tetrazine molecule. The decaytimes of the different vibronic levels are represented in fig. 3.4 and will be discussed.
For the rotational structure s-tetrazine can be described as an oblate symmetrical-top molecule.

2. Collision-induced vibrational energy flow in s-Tetrazine.

Fluorescence studies of S-T vapour with added foreign gases at different pressures are used to follow the level to level energy flow. Because of the short lifetimes of the excited states it is possible to perform measurements of the fluorescence spectra at pressures where not more than one hard sphere collision has occurred. Hence intramolecular relaxation channels can be followed as a result of one single collisional step.
The fluorescence spectra obtained after excitation of single vibronic levels are simple as stated in the preceeding section and the vibrational structure of these spectra is well resolved so that the relative intensities of the various emission bands can be determined accurately. As an example we will

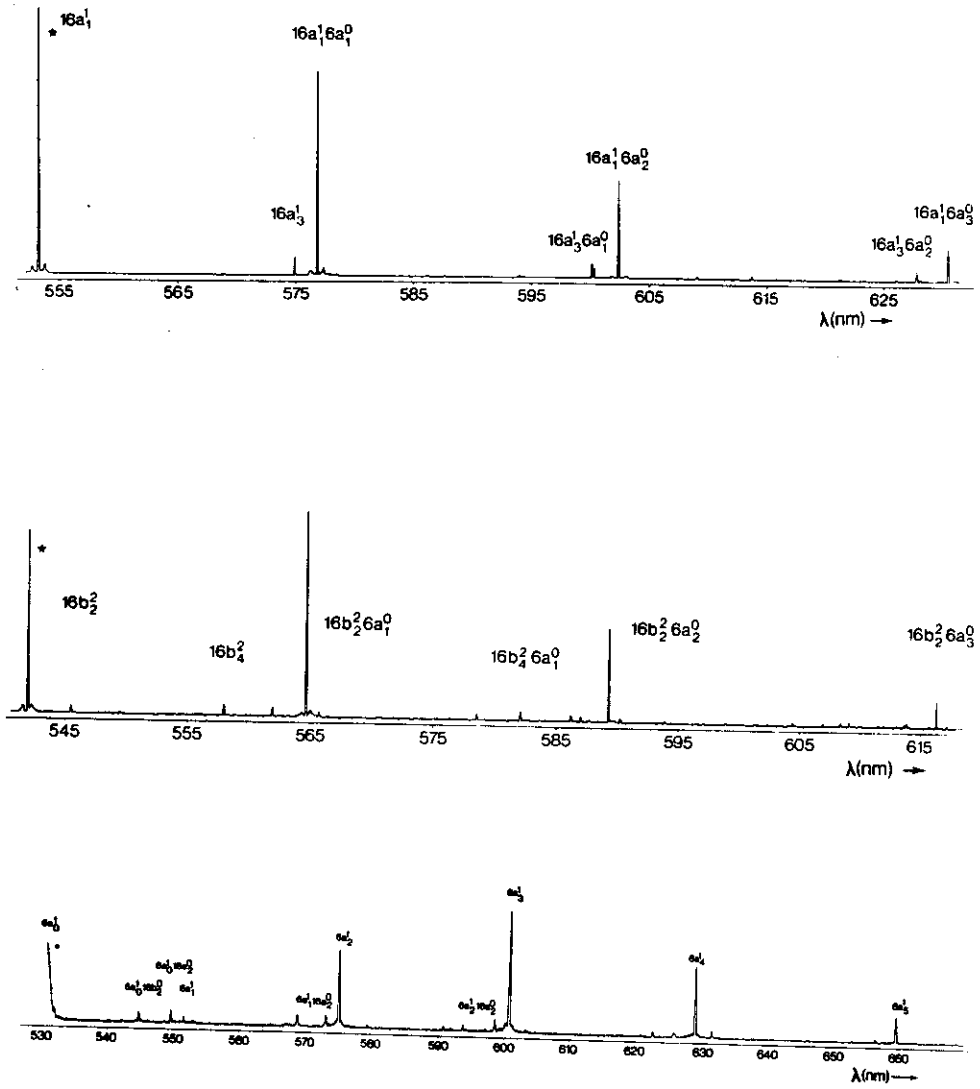

Fig. 3.3. Emission spectra of the levels $16a^1$, $16b^2$ and $6a^1$ of s-tetrazine (0.5 Torr) after excitation of the absorption transition indicated with an asterix.

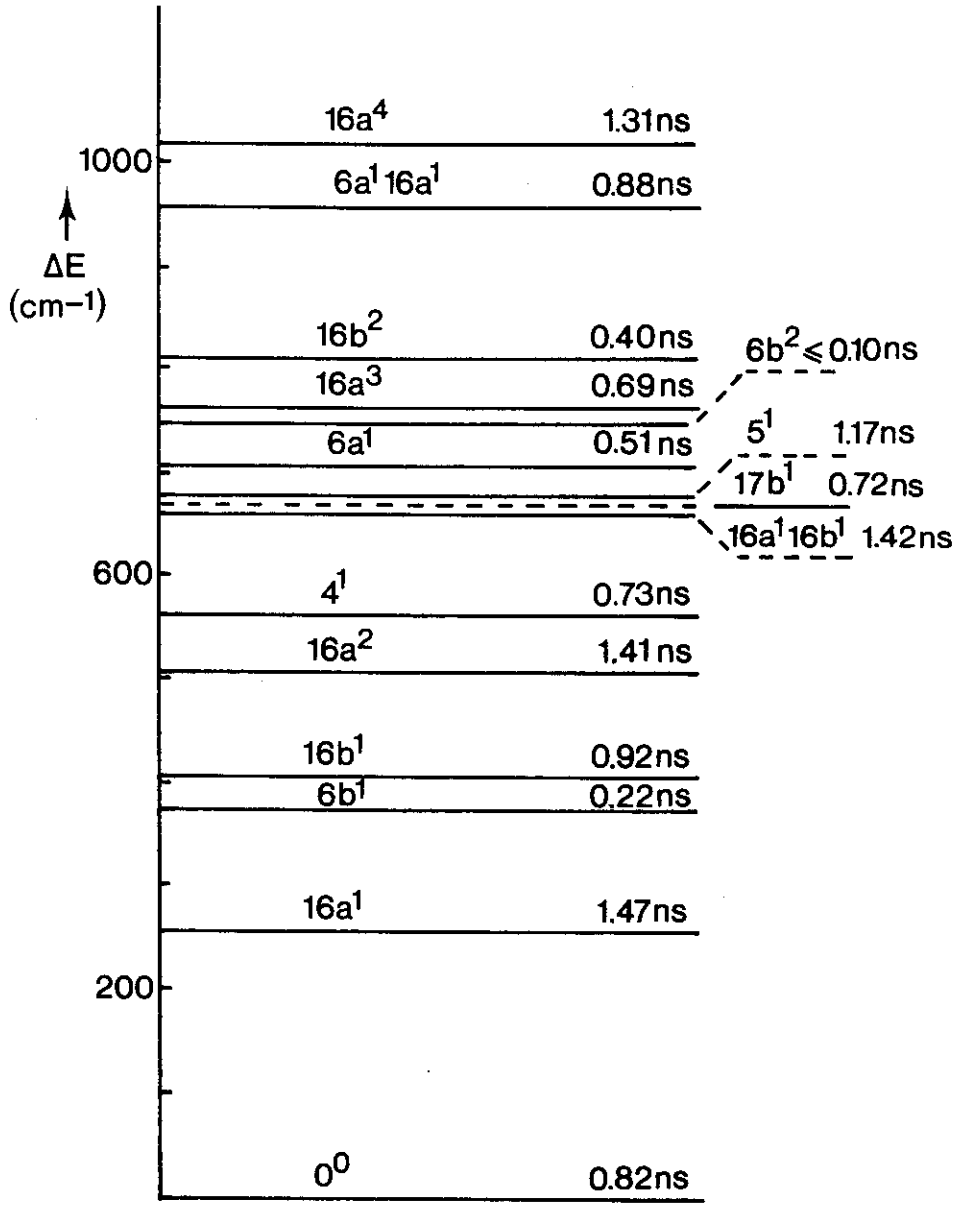

Fig. 3.4. Fluorescence decay times of low lying vibronic levels of s-tetrazine at 1 mbar.

focus our attention in this lecture on the vibrational deactivation of the combination level $16a^1 16b^1$. A part of the emission spectrum originating from this level is shown in Fig. 3.5a This spectrum was obtained after excitation into the $16a_1^1 16b_1^1$ band at a vapour pressure of 0.5 torr. Fluorescence decay measurements show that the collision-free lifetime of this level varies between 1420 and 1900 ps dependent on the rotational quantum numbers.

The spectra shown in Figs. 3.5b and c were measured at a pressure of 125 torr He and 500 torr Xe respectively. The resonance bands are due to emission from the pumped level $16a^1 16b^1$ and the new emission bands, which are absent in Fig. 3.5a, can be ascribed to transitions originating from the levels $16a^2$, $16a^1$, $16b^1$ and 0^o.

Fig. 3.6 shows the levels to which vibrational energy transfer out of $16a^1 16b^1$ can be observed under single collision condidions.

Accurate time-resolved experiments of vibrational relaxation, specially of the population growth of the relaxed levels, are not meaning full because of the variation of the lifetime with rotational energy. These experiments will be discussed in the molecular jet results of Van der Waals complexes in Chapter IV.

3. Molecular jet spectra of s-Tetrazine.

For a description of the use of a molecular beam in spectroscopy the reader is referred to the lectures of Prof. A. Dymanus. We used for our experiments a supersonic expansion of argon gas seeded with ∿ 0.03% s-tetrazine. The expansion was conducted through a nozzle of 50 or 100 um with an Ar stagnation pressure between 1 and 1.5 bar. For the time and spectrally resolved emission we used the equipment as described in chapter II. The change of the velocity distribution of the molecules in the supersonic jet is defined by a temperature with help of a Maxwell-distribution. The relative velocity between the particles-decrease as a function of the distance to the nozzle.

For the translational temperature this is presented in fig. 3.7 (T_o= 300K, nozzle diam. 230 um).

Fig. 3.5. a. Resonance fluorescence from level $16a^1 16b^1$ measured at a pressure of 0.5 torr. Figs. b and c show the same part of the spectrum after addition of 125 torr of helium and 500 torr of xenon respectively. Because of the large variations in the relative intensities of the emission bands, different parts of the spectrum have been recorded with different attenuation factors. These factors are given in the figure.

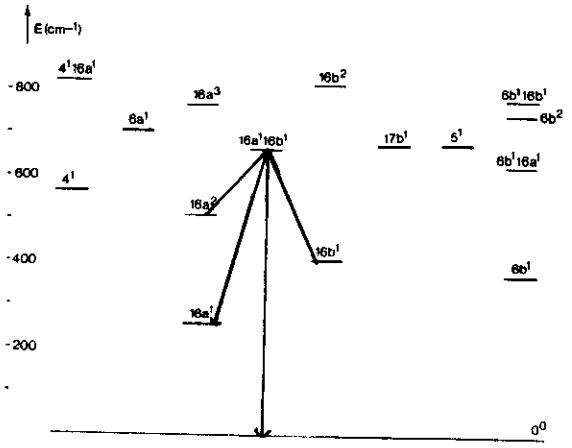

Fig. 3.6. Position of vibronic levels of s-tetrazine up to 800 cm^{-1} above the vibrationless level of the S_1-state. The arrows indicate the collision-induced vibrational energy transfer from level $16a^1 16b^1$ to levels which are populated by a single collision.

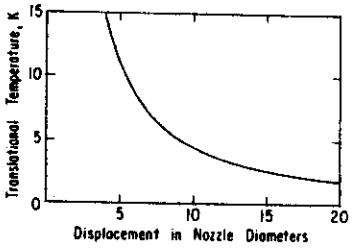

Fig. 3.7. T_{tr} vs. distance to the nozzle (in nozzle diameters).

For vibrational levels the cooling is dependent on the normal mode. We therefore have to define a vibrational temperature (T^{eff}_{vibr}) for each normal mode.
It is expected that normal modes with low frequency are better cooled than others having a higher frequency.
Even in the collision free region of the jet for the lowest vibrational energy modes a $T^{eff}_{vibr} \geq 100$ K is expected.
The collision free region is reached after about 10 nozzle diameters for s-Tetrazine. The fluorescence excitation and emission spectra of the $6a^1$ molecular level are presented in fig. 3.8. The results show that collision induced vibrational relaxation at the molecular jet conditions are not observed.

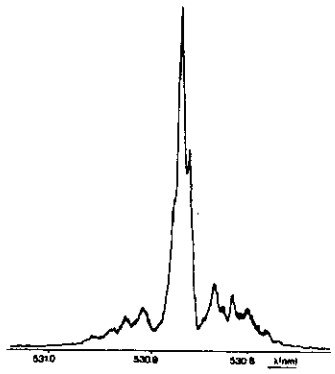

Fig. 3.8.a. Fluorescence excitation spectrum of the $16a^1_0$ s-tetrazine molecular transition in a supersonic jet.

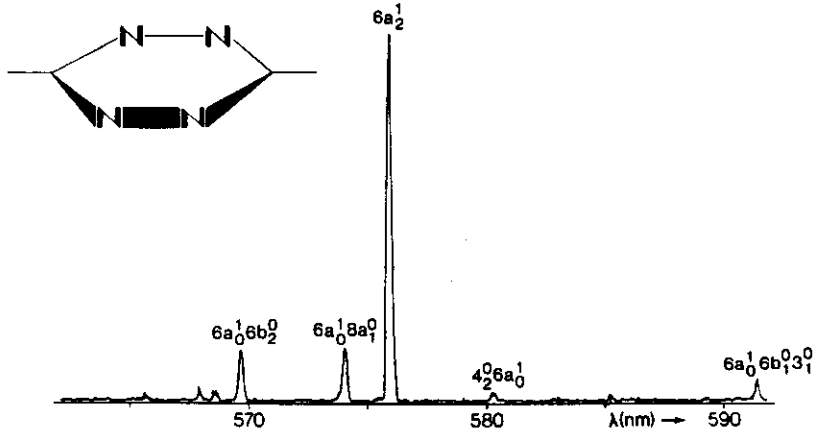

Fig. 3.8.b. Part of the fluorescence emission spectrum of the $6a^1$ level of the s-tetrazine molecule. Note: all emission is from the $6a^1$ level.

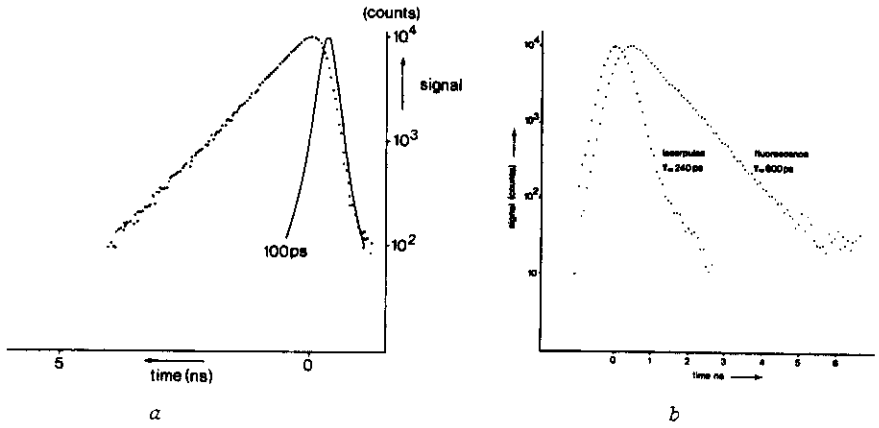

Fig. 3.9. Fluorescence decay curves of s-tetrazine in a supersonic jet;
a. with a laserpulse of 7 ps (FWHM) giving an 1/e decay response of ∿ 100 ps.
b. with a laserpulse of 720 ps (FWHM, $\Delta\nu \approx 0.02$ cm^{-1}) giving an 1/e decay response of ∿ 240 ps.

For the decaytimes of the molecular levels (fig. 3.9) the same lifetime is observed as at room temperature (fig. 3.4). The kinetic considerations will be discussed in the next chapter for s-Tetrazine-Ar Van der Waals molecules.

IV. S-TETRAZINE-Ar VAN DER WAALS MOLECULES.

1. Consecutive vibrational redistribution and predissociation processes.

S-Tetrazine argon complexes T-Ar_n (n=1,2) are formed in a supersonic expansion of argon seeded with s-tetrazine. The expansion was conducted through a nozzle of 50 of 100 μm with an argon stagnation pressure between 1 and 1.5 bar. From spectrally resolved measurements it is clear that vibrational redistribution processes as well as vibrational predissociation processes take place after SVL excitation within the complex.

From rise and decay time experiments it can be concluded, that after excitation of the $6a^1$ complex level, the above mentioned processes are consecutive and not parallel. It appears that the out of plane mode 16a couples with the Van der Waals stretching mode. The predissociation rate of the $16a^2$ complex is observed to be $2.3 \times 10^9 s^{-1}$.

This section will be discussed on the basis of the following preprint.

CONSECUTIVE VIBRATIONAL REDISTRIBUTION AND PREDISSOCIATION PROCESSES IN S-TETRAZINE-ARGON VAN DER WAALS COMPLEXES.
Authors: J.J.F. Ramaekers, L.B. Krijnen, H.J. Lips, J. Langelaar and R.P.H. Rettschnick.

Lasers in Chemistry, 1983 (in press)
Contents: Introduction; Supersonic jet spectroscopy; Kinetics.

2. Special topics concerning s-Tetrazine and its Van der Waals complexes.

In this lecture a selection of special topics will be made on the basis of the students interest and the available time. The student is referred to the Appendix A-I which contains a preprint of the paper "Energy conversion in Van der Waals complexes of s-Tetrazine and Argon", Faraday Disc. Chem. Soc. (1983) (in press).

Preprint from: Lasers in Chemistry (in press, 1983), J.J.F. Ramaekers et al.

INTRODUCTION

In a supersonic expansion of s-tetrazine seeded in argon, Van der Waals-complexes are created during the cooling process. The weakly bound complexes are stable in the region after the nozzle and can thus be studied by laser induced excitation and fluorescence spectroscopy [1,2,3]. The T-Ar_n (n=1,2) complexes as well as the parent molecule tetrazine can be studied in the supersonic jet under identical conditions by selective excitation. A good comparison then is possible with the known SVL spectra of s-tetrazine in a vapour at room temperature under isolated conditions and in the single collision regime [4,5]. After SVL excitation of the complexes, resonance emission from the prepared level is observed in combination with vibronic level emission from other modes which is attributed to either complex emission or to emission from the parent molecule [2,3]. In this paper we will attribute these results to vibrational relaxation and vibrational predissociation processes. The different channels are followed in time by means of fast decay and rise time experiments. The characterization of the fluorescence emission and excitation spectra is available in literature [1,4,5]. In a vapour at room temperature (0.5 torr) no vibrational relaxation processes are observed in the different vibrational levels studied. On the other hand the decay times observed in the excited state for the different single vibronic levels up to 1000 cm^{-1} change from < 100 ps up to 1.5 ns. It is assumed that this is due to internal conversion processes followed by photochemical decomposition.

SUPERSONIC JET SPECTROSCOPY

In the supersonic jet experiments with a nozzle diameter of 50 and 100 μm and an Ar stagnation pressure of 1.2 bar with 0.03% s-tetrazine vibrational relaxation processes in the tetrazine molecule itself are not observed (i.e. $\leq$ 0.5%) in a region after the nozzle from 0 to 5 mm. The dimension of the area excited by the synchronously pumped CW dye laser and observed by a high resolution monochromator in all experiments was of the order of 50 x 50 μm.

In contrast to the observation with the molecular species we observed efficient vibrational relaxation and vibrational predissociation effects when the Ar Van der Waals complex species were excited under the same conditions. We have assumed [3] that soft collisions or orbiting collisions are efficient to induce vibrational relaxation in the s-tetrazine-Ar complex assisted by perturbation of the molecular vibration by the Van der Waals bound Ar atom.

Dispersed fluorescence spectra are obtained with narrow band laser excitation ($\Delta\sigma \approx 0.1$ cm^{-1}) by means of a 1.5 meter J.Y. grating monochromator (0.24 nm/mm) at a resolution of 1 cm^{-1}. Fluorescence excitation and emission spectra were measured for the 0^0, $16a^2$, $6a^1$ and $6b^2$ levels of the molecular and complex species. The fluorescence excitation spectrum which reveals the 0^0_0 transition of the T-Ar complex shifted -23 cm^{-1} with respect to the molecular transition is presented in reference [6]. Blue shifted bands at 34 and 38 cm^{-1}, and 43 cm^{-1} from the T-Ar complex band are attributed to resp. the Van der Waals bending (2x) and stretching modes.

Dispersed fluorescence emission spectra of the T-Ar complexes were obtained for the single vibronic levels $\overline{0^0}$, $\overline{16a^2}$, $\overline{6a^1}$ and $\overline{6b^2}$. (The complex levels and transitions are indicated by a bar above the molecular level notation.)

The spectra could be well compared with the known resonance emission spectra of the parent molecule [4]. The emission spectra of the molecular species and the complex species which have to be compared, were run under the same conditions in the cold molecular jet. The results will be discussed. For each transition, the main observed emission bands are represented in tables I-IV. The full interpretation of the results will be discussed elsewhere [6]. The main SVL emission bands of T-Ar after $\overline{0_0^0}$ excitation are given in table I.

The main transitions from the spectra of tetrazine-argon after $\overline{16a_0^2}$, $\overline{6b_0^2}$ and $\overline{6a_0^1}$ excitation are summarized in table II, III and IV respectively. Relative fluorescence intensities are presented in these tables for the appropriate excitation wavelengths. It is worth noticing that the relative fluorescence intensities are strongly dependent on the excitation wavelength within the broad (3 cm^{-1}, FWHM) excitation band of the particular transition within the complex.

A comparison with the resonance emission of the parent molecule shows that several vibrational levels are populated in the complex as a result of intermolecular or intramolecular vibrational relaxation.

The emission spectra of $6a^1$ T-Ar and T-Ar_2 were published in ref. [3]. In figure 1 we present the emission spectrum after $\overline{6b_0^2}$ excitation. The results given in table III and IV both for $\overline{6b_0^2}$ as well as for $\overline{6a_0^1}$ excitation indicate, that as a result of vibrational relaxation within the complex, mainly the $\overline{16a^2}$, $\overline{16a^1 16b^1}$ and $\overline{5^1}$ levels are formed.

Vibrational predissociation, a relaxation process of the complex with ejection of the argon atom, mainly produces tetrazine in the $16a^1$ and $16b^1$ level.

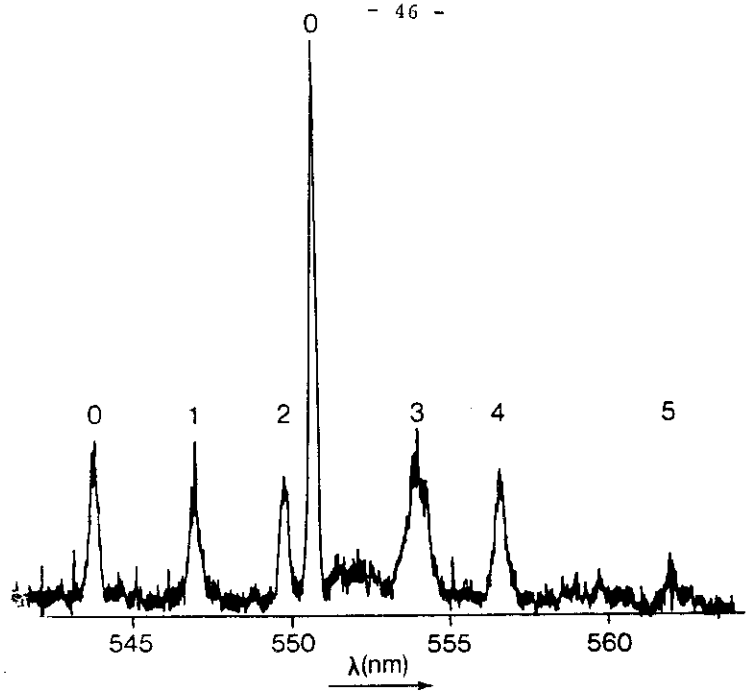

Fig. 1a. Part of the fluorescence emission spectrum of the s-tetrazine argon complex after $\overline{6b_0^2}$ excitation. (18889 cm^{-1}). Detection bandwidth = 10 cm^{-1}.

0: Resonance emission
1: $\overline{16b^1}$ emission
2: $\overline{16a^1 16b^1}$ emission
3: $\overline{16a^1}$ emission
4: $\overline{16a^2}$ emission
5: $\overline{5^1}$ emission

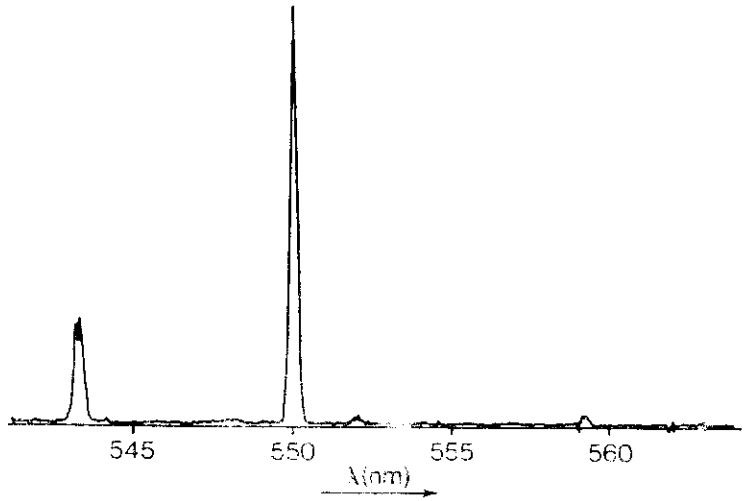

Fig. 1b. Part of the fluorescence emission spectrum of the s-tetrazine [illegible] after $\overline{6b_0^2}$ excitation. (18912 cm^{-1}). Detection bandwidth = 10 cm^{-1}.
[illegible] emission originates from the [illegible]

Table I. Main bands of the $\overline{0^0}$ fluorescence spectrum of T-Ar (Excitation: 0_0^0, 18105 cm^{-1}).

OBSERVED FREQUENCY	RELATIVE INTENSITY	ASSIGNMENT T	ASSIGNMENT T-Ar
17370	100		$6a_1^0$
17338	1.2		$6a_1^0 (\beta_y)_1^0 + 6a_1^0 (\beta_z)_1^0$
17328	1.5		$6a_1^0 (\sigma_x)_1^0$
16635	63		$6a_2^0$
16603	0.4		$6a_2^0 (\beta_y)_1^0 + 6a_2^0 (\beta_z)_1^0$
16593	0.8		$6a_2^0 (\sigma_x)_1^0$

Table II. Part of the emission bands of T-Ar after excitation in the $\overline{16a_0^2}$ transition at 18630 cm^{-1}. (It is inevitable that also the molecular transition $16a_0^2$ is excited).

OBSERVED FREQUENCY	RELATIVE INTENSITY	ASSIGNMENT T	ASSIGNMENT T-Ar
17967	239	$16a_2^2$	
17960	100		$16a_2^2$
18046	111	$16a_1^1$	$(16a_1^1)$
18128	45	0_0^0	
18263	8		$16b_1^1$

Table III. Part of the emission bands of T-Ar after excitation of the $\overline{6b^2}$ level (18889 cm^{-1}).

OBSERVED FREQUENCY	RELATIVE INTENSITY	ASSIGNMENT T	ASSIGNMENT T-Ar
18388	32		$6b_0^2\ 16b_2^0$
18280	32	$16b_1^1$	
18187	30		$16a_1^1\ 16b_1^1$
18157	100		$6b_0^2\ 6a_1^0$
18048	77	$16a_1^1$	
17962	40		$16a_2^2$
17790	10		5_1^1

Table IV. Part of the emission bands of T-Ar after excitation of the $\overline{6a^1}$ level (18809 cm^{-1}).

OBSERVED FREQUENCY	RELATIVE INTENSITY	ASSIGNMENT T	ASSIGNMENT T-Ar
18765			$6a_0^1 (\sigma_x)_1^0$
18304	14		$6a_0^1\ 16b_2^0$
18268	4		$16b_1^1$
18182	13		$16a_1^1\ 16b_1^1$
18138	16		$6a_0^1\ 16a_2^0$
18123	2		
18073	8		$6a_1^1$
18048	99	$16a_1^1$	
18008	2		$6a_0^1\ 4_1^0$
17961	37		$16a_2^2$
17894	2		
17862	1		
17855	1		$6a_0^1\ 1_1^0$
17799	2		
17787	7		5_1^1
17585	2		$6a_0^1\ 16a_1^0\ 16b_1^0\ 6b_1^0$
17565	3		$6a_1^1\ 16b_2^0$
17528	13		$6a_0^1\ 6b_2^0$
17446	10		$16a_1^1\ 16b_1^1\ 6a_1^0$
17404	3		$6a_1^1\ 16a_2^0$
17394	17		$6a_0^1\ 8a_1^0$
17370	9	$16a_3^1$	
17337	100		$6a_2^1$
17312	86	$16a_1^1\ 6a_1^0$	
17294	2		$6a_2^1 (\sigma_x)_1^0$
17279	6		$16a_4^2$
17226	26		$16a_2^2\ 6a_1^0$
17207	3		$6a_0^1\ 4_2^0$
17142	2		

KINETICS

In addition to the spectra, we have performed time resolved experiments to analyse the individual kinetics and to deduce whether the different processes are taking place parallelly or are consecutive.
In this paper we will analyse the results obtained for the T-Ar complex excited in the $\overline{6a^1}$ and $\overline{16a^2}$ level.
After excitation in the $\overline{6a^1}$ level the emission spectrum tells us that the vibrational energy mainly flows to the $\overline{16a^2}$ mode of the complex and to the $16a^1$ mode of the molecular species.
The first process

$$\overline{6a^1} \rightarrow \overline{16a^2} \qquad (1)$$

must be due to vibrational redistribution; the second process due to vibrational predissociation either from the $\overline{6a^1}$ level directly i.e.

$$\overline{6a^1} \rightarrow 16a^1 + Ar \qquad (2)$$

or from a consecutive process of process (1) i.e.

$$\overline{16a^2} \rightarrow 16a^1 + Ar \qquad (1a)$$

A first indication is obtained from the graphically determined decay times for the three levels, as compared with the decaytimes of s-tetrazine in the same vibrational levels (table V).

Table V . Graphically determined decay times (ps) for several levels

s-Tetrazine		T-Ar (after exc in $\overline{6a^1_0}$)		T-Ar (after exc in $\overline{16a^2}$)	
$6a^1$	520	$\overline{6a^1}$	520		
$16a^2$	1540	$\overline{16a^2}$	∿ 600	$\overline{16a^2}$	∿ 800
$16a^1$	1450	$16a^1$	1500	$16a^1$	1400

In the $6a^1$ level a similar decay time is observed for excitation of the molecule and for the argon complex. This indicates that the processes (1) and (2) do not compete with the main deactivation process, i.e. the photodissociation of s-tetrazine into its products HCN and N_2. For the $\overline{16a^2}$ level we see a drastic reduction of the decay time indicating that the predissociation process ($_{1a}$) is an extra channel competing with the photodecomposition of the molecule.
A similar reduction in decaytime is observed after direct excitation of the $\overline{16a^2}$ level of the complex. Here the predissociation channel

$$\overline{16a^2} \rightarrow 16a^1 + Ar \qquad (3)$$

also reduces the decay time of the $\overline{16a^2}$ level. In order to proof these interpretations we performed risetime experiments for the different levels mentioned in the processes (1) to (3). For this we used a fast cross-field photomultiplier with a risetime of 80ps (10 to 90%). Unfortunately the decay time of this detector was not as fast as its rise-time, the cause of which is not understood yet. It will, however, not influence the decay times presented in this paper.

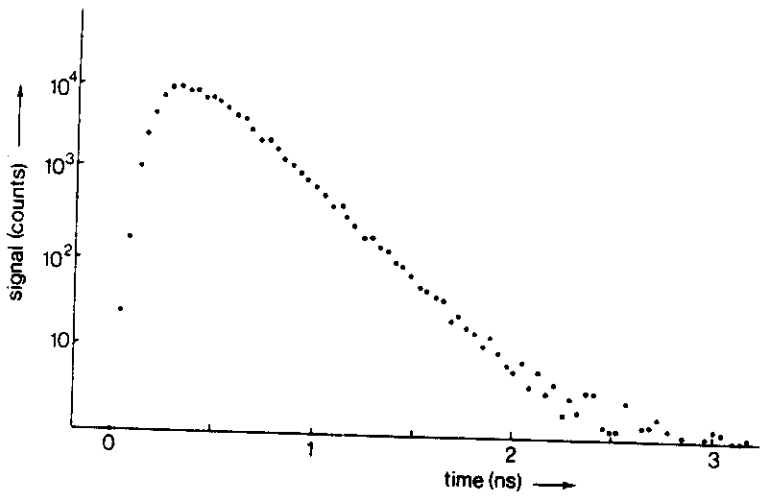

Fig. 2. Experimental growth and decay curve of the $\overline{6a^1}$ fluorescence emission after excitation within the $6a_0^1$ band of the s-tetrazine-argon Van der Waals complex. Decaytime $\tau(\overline{6a^1})$ = 520 ps.

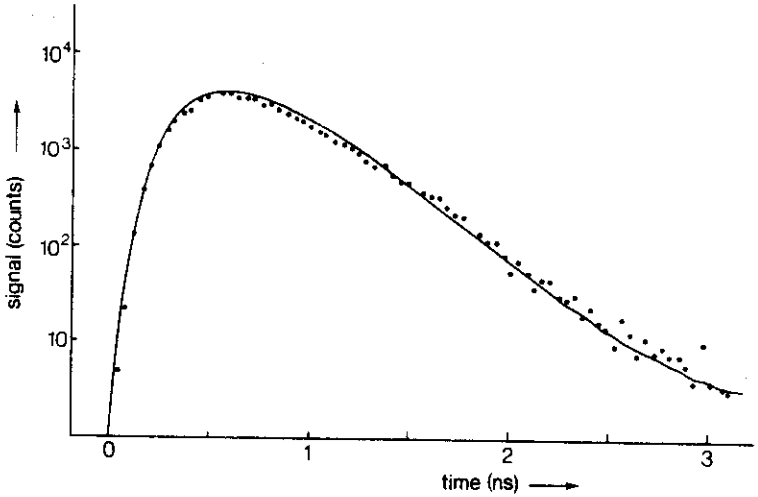

Fig. 3. Dotted curve: Experimental growth and decay curve of the $\overline{16a^2}$ emission after $6a_0^1$ excitation.
Drawn curve: Best fit computer simulation for this emission using the experimental curve of fig. 2 as input.
Process: $6a^1 \rightarrow \overline{16a^2}$; Decaytime $\tau(\overline{16a^2})$ = 330 ps.

The growth and decay of the prepared $\overline{6a^1}$ level of the T-Ar complex was measured and is represented in fig. 2 (dotted curve). The observed growth of this resonance emission equals the risetime of the detector and electronics, because the excitation was performed with a short (7ps, FWHM) pulse from the synchronously pumped dye laser. The decay time obtained for the $\overline{6a^1}$ complex level is 520 ps, similar to that observed for the molecular species in the $6a^1$ level (table V).

The experimental growth and decay curve of the formed $\overline{16a^2}$ level is represented in fig. 3 (dotted curve). If we assume, according to process (1), that the $\overline{16a^2}$ level is formed directly from the excited $\overline{6a^1}$ level, then the growth and decay has to be a convolution of the pulseform of the $\overline{6a^1}$ emission with the decay time of the $\overline{16a^2}$ level. The best fit with the experimental curve is obtained with a decay time of 330 ps. (fig. 3, drawn curve). It is worth to mention here that this decay time is a factor of 2 shorter than that graphically obtained from the logarithmic plot of the experimental curve, not taking into account the growth and decay of the level from which it is formed as is the case for the numbers given in table V and ref. [3].

Finally the growth and decay of the $16a^1$ level was measured and compared with the calculated curve as if it was formed either by process (1a) or by process (2). If the $16a^1$ level is formed according to the predissociation process (1a) than a convolution of the pulseform of the $\overline{16a^2}$ emission with the appropriate $16a^1$ decay time has to give the best fit between calculated and experimental curve. If on the other hand process (2) is the correct channel for the predissociation process than the convolution has to be carried out with the pulseform of the $\overline{6a^1}$ emission. The best fit is obtained in agreement with process (1a) (fig. 4). Hence the results indicate that process (2) can

be neglected, which brings us to the conclusion that predissociation of the T-Ar complex does not take place directly from the prepared $\overline{6a^1}$ level.

On the other hand vibrational predissociation is appreciable from the $\overline{16a^2}$ level of the complex. We might conclude that a s-tetrazine argon complex prepared in an in-plane vibrational mode $\overline{6a^1}$ first has to redistribute its vibrational energy to an out of plane $\overline{16a^2}$ complex mode before it predissociates to a molecular species in the $16a^1$ level and an argon atom. Hence vibrational relaxation and vibrational predissociation of a Van der Waals complex are consecutive processes and do not take place parallelly from the prepared $\overline{6a^1}$ level. From the results presented in figure 3 we calculate a vibrational predissociation rate of $2.3 \times 10^9 s^{-1}$ for the $\overline{16a^2}$ level. A similar result is obtained by kinetic studies of the $\overline{16a^2}$ level after direct excitation of the $\overline{16a_0^2}$ band. Clearly, a coupling between the out of plane 16a mode of s-tetrazine and the Van der Waals stretching mode ($43\ cm^{-1}$) is also illustrated by the results presented in this paper (see also ref [6]).

ACKNOWLEDGEMENT

The authors are indebted to Mr. D. Bebelaar for developing the fast detection equipment. The investigations were supported in part by the Netherlands Foundation for Chemical Research (SON) with financial aid from the Netherlands Organization for Advancement of Pure Research (ZWO).

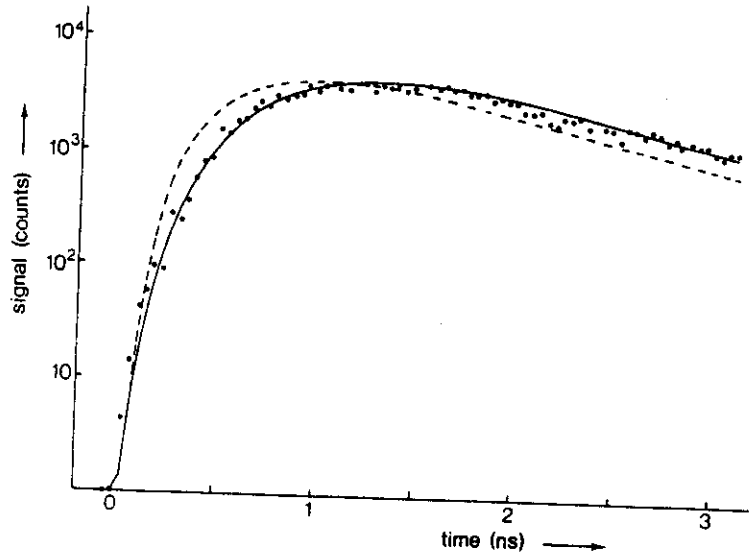

Fig. 4. Dotted curve: Experimental growth and decay curve of the $16a^1$ emission after $6a_0^1$ excitation.
Drawn curve: Best fit computer simulation for the $16a^1$ emission using the drawn curve of fig. 3.
Process: $16a^2 \rightarrow 16a^1$; Decaytime $\tau(16a^1) = 1450$ ps.
Dashed curve: Computer simulation for $16a^1$ emission using the curve of fig. 2 as input. A good fit cannot be obtained.
Process: $6a^1 \rightarrow 16a^1$; Decaytime $\tau(16a^1) = 1450$ ps.

REFERENCES

1. R.E. Smalley, L. Wharton and D.H. Levy, J.Chem.Phys. 68, 2487 (1978).

2. J.E. Kenny, D.V. Brumbaugh and D.H. Levy, J.Chem.Phys. 71, 4757 (1979).

3. J.J.F. Ramaekers, J. Langelaar and R.P.H. Rettschnick, Picosecond Phenomena III, Ed. K.B. Eisenthal, R.M. Hochstrasser, W. Kaiser, A. Laubereau, p. 264-268, Springer Verlag (1982).

4. M.W. Leeuw, Thesis, University of Amsterdam (1981); M.W. Leeuw, J. Langelaar and R.P.H. Rettschnick, Proc.of the UPS 80, Reinhardsbrunn DDR, p. 220-224 (1980).

5. D.V. Brumbaugh and K.K. Innes, Chem.Phys. 59, 413 (1981).

6. J.J.F. Ramaekers, H.K. van Dijk, J. Langelaar and R.P.H. Rettschnick, Farad. Disc. Chem. Soc. (in press).